A TIME-DIFFERENTIAL PERTURBED ANGULAR CORRELATION STUDY OF K_3HfF_7

By

© IAN ALEXANDER CUNNINGHAM, B.Sc.

A Thesis
Submitted to the School of Graduate Studies
in Partial Fulfilment of the Requirements
for the Degree
Master of Science

McMaster University
September 1981

A PERTURBED ANGULAR CORRELATION
STUDY OF K_3HfF_7

MASTER OF SCIENCE (1981)
(Physics)

McMaster University
Hamilton, Ontario

TITLE: A Time-Differential Perturbed Angular Correlation Study of K_3HfF_7

AUTHOR: Ian Alexander Cunningham, B.Sc. (Queen's University)

SUPERVISOR: Dr. W.V. Prestwich

NUMBER OF PAGES: xii, 100, II

ABSTRACT

The method of using time dependent perturbed angular correlations (TDPAC) is used in a study of the hafnium atom's environment in K_3HfF_7. It is found that there are two possible electric field gradients (EFG), different in both magnitude and asymmetry about the axis of the greatest component, at sample temperatures below 250 ± 1 Kelvin and only one above. This indicates that a solid to solid phase transition occurs at this temperature from a two site structure for the hafnium to a one site form. The EFG asymmetry of the low temperature site, having a relative population of 0.25, increases from 0.62 ± .03 to >.95 between 170 and 230 Kelvin. This can be interpreted as the effect of a second state of this hafnium site with an energy difference of approximately 0.25 eV and a relative degeneracy of approximately 10^{-7}. Such a state could be the result of an impurity or lattice distortion.

Using the K_3HfF_7 as a sample study, the observed data was operated on in a deconvolution analysis to remove the effect of the finite time response of the measurement apparatus. An iterative Bayesian approach was found to amplify high frequency spectral noise less than the linear inverse filter technique however the noise inherent in the

measured data limits the usefulness of this type of analysis. The parameters used to describe the EFG interaction, evaluated in a least squares fit of the theoretical expression to the data, were found to be unaffected by the deconvolution operation within statistical uncertainties.

ACKNOWLEDGMENTS

It is a pleasure to acknowledge the assistance and guidence I have received during my work at McMaster University from my research supervisor, Dr. W.V. Prestwich. I am indebted to him for the many ideas and generous assistance he has offered with undying patience. I would also like to acknowledge Dr. T.J. Kennett for his helpful comments and leadership in many aspects of this work and the other members of my supervisory committee, Dr. J.A. Kuehner and Dr. W.B. Clarke.

It is impossible to properly credit everyone who has made a contribution or given support during the preparation of this thesis. I would however like to thank Kenrick Chin for his technical expertise and my fellow students, Tom Cousins, Diane Lowe and Richard Tervo, for helping to make my stay at McMaster an enjoyable one.

TABLE OF CONTENTS

Chapter Page

1.0 INTRODUCTION 1

2.0 THE THEORY OF PERTURBED ANGULAR CORRELATIONS 5

2.1 Angular Correlations 5

2.2 The Unperturbed γ-γ Angular Correlation 6

2.3 The Perturbed Differential γ-γ Angular Correlation 9

2.3.1 The Static Electric Quadrupole Interaction 11

2.3.2 The Dynamic Electric Quadrupole Interaction 12

2.3.3 The Effect of a Finite Distribution in V_{zz} 15

3.0 DESCRIPTION OF THE EXPERIMENT 19

3.1 The Hafnium Source 19

3.1.1 Sample Preparation 21

3.2 The Sample Chamber 21

3.3 Sample Temperature Control 23

3.4 The Detectors : Time Resolution Considerations 27

3.5 The Electronic Arrangement for Coincident Counting 29

Chapter Page

4.0 INSTRUMENTAL EFFECTS INFLUENCING THE MEASURED PERTURBATION FACTOR 34

4.1 Finite Time Resolution : System Response 34

4.2 Finite Detector Solid Angle 38

4.3 Time Scale Calibration 39

4.4 Accidental Coincidences (Background) 42

5.0 DATA ANALYSIS 44

5.1 The Fourier Transform 45

5.2 An Alternative Fourier Transform Using a Weighted Least Squares Approach 46

5.3 The Convolution Integral 49

5.4 Deconvolution Techniques 51

5.4.1 Deconvolution for the Time Zero Channel 56

5.4.2 Deconvolution of the Perturbation Factor 61

6.0 EXPERIMENT RESULTS 69

6.1 Calculation of the Perturbation Factor 69

6.2 Results of the Fourier Analysis 69

6.3 Results of the Deconvolution Analysis 73

6.4 Results of the Least Squares Fitting Analysis 76

6.5 Discussion 86

Chapter Page

7.0 CONCLUSIONS 96

8.0 BIBLIOGRAPHY 98

9.0 APPENDIX I : THE QUADRUPOLE INTERACTION HAMILTONIAN I-1

10.0 APPENDIX II : SIMULATION OF AN ELECTRIC FIELD GRADIENT FROM A POINT CHARGE DISTRIBUTION II-1

LIST OF ILLUSTRATIONS

Figure	Title	Page
2-1	The parity and angular momentum of a nucleus for a gamma-gamma cascade decay.	8
2-2	A two detector arrangement used to observe the angular gamma-gamma correlation.	8
2-3	The I=5/2 state is split into the degenerate Zeeman levels.	13
2-4	The splitting of the Zeeman levels as a function of η, the asymmetry parameter.	13
2-5	The perturbation factor, $G_2(t)$, for $\eta=0$, .33, .67 and 1.0 with $\delta=0$.	14
2-6	The perturbation factor, $G_2(t)$, for $\delta=0$, 0.1 and 0.4 with $\eta=0$.	17
3-1a	The gamma spectrum of ^{181}Hf obtained with a Ge(Li) detector.	20
3-1b	The decay scheme of ^{181}Hf.	20
3-2	Cut-away view of the sample chamber.	22
3-3	Schematic of the temperature control circuit.	24
3-4	Schematic of the feedback control circuit.	25
3-5	The three detector fast-slow coincidence circiut.	31
4-1	The system response function measured directly with a ^{22}Na source.	35
4-2	The system response function calculated indirectly from a measured data spectrum.	37
4-3	Time scale calibration spectrum.	41

Figure	Title	Page
5-1	A waveform in the time domain and its transform in the frequency domain.	47
5-2	A comparison of the weighted least squares Fourier transform with the discrete fast Fourier method for a data set with a time dependant noise component.	50
5-3	Simulation of an observed data spectrum by convolving the true data with a gaussian response function.	52
5-4	Bayesian deconvolution of a simulated spectrum.	55
5-5	Comparison of the linear inverse filter deconvolution with the Bayesian approach.	57
5-6	Time zero alignment error as a function of the Bayesian iteration index.	59
5-7	The perturbation factor calculated with and without the extra one channel shift of the 180° time-interval spectrum.	60
5-8	The simulated perturbation factor is convolved and then deconvolved with 16 iterations of the Bayesian technique.	62
5-9	Frequency response of the convolution / deconvolution process as a function of the frequency-time resolution product.	64
5-10	Factor of improvement in the effective time resolution from the Bayesian deconvolution process.	65
5-11	Noise properties of deconvolved spectra.	67
6-1	Sample time-interval spectra.	70
6-2	Frequency power spectra of the perturbation factors using the weighted least squares technique.	72
6-3	Deconvolution of measured perturbation factors.	74

Figure	Title	Page
6-4a	Measured perturbation factors from 138 to 245 K.	78
6-4b	Measured perturbation factors from 248 to 318 K.	79
6-5	The fitted fundamental frequency.	80
6-6	The population probability of site A.	81
6-7	The fitted asymmetry parameter.	82
6-8	The fitted frequency spread.	83
6-9	The relaxation parameter.	84
6-10	The calculated quadrupole frequency.	85
6-11	The distorted pentagonal bipyramidal structure of HfF_7^{3-}.	90
6-12	Distributions in the EFG and interaction frequencies for the distorted bipyramidal model.	91
6-13	Comparison of measured site B asymmetry with the two state model.	94

LIST OF TABLES

Table	Title	Page
4-1	The angular correlation factors A_k corrected for finite detector width.	40
6-1	Comparison of experiment results with previous studies.	87

CHAPTER 1

INTRODUCTION

The method of using perturbed angular correlations (PAC) is one of several available to researchers for studying the internal structure of materials. It can be used as a complementary tool to the Mossbauer technique, and sometimes to the nuclear magnetic resonance technique, for determining the nature of the hyperfine interaction between nuclear electromagnetic moments and extranuclear electromagnetic fields. In the area of solid state physics or physical chemistry this enables an investigator to study properties of the electric field gradient and/or the magnitude of a magnetic field at the site of a probe isotope, of which there are known to be approximately twenty-five suitable to this technique.

As the name implies, this effect is a perturbation of the more commonly studied angular correlation in the decay of an unstable nucleus. In general it is a time-dependent perturbation and is often given the abbreviated title TDPAC. It can be observed experimentally by measuring the distribution of time intervals between successive emissions in a gamma-gamma cascade as a function of the emission angle. Alpha-gamma and beta-gamma PAC interactions are also possible but are not delt with in this study.

The TDPAC technique is not new; the first experiment was performed in 1951 by Frauenfelder (Fr51). The theory was first treated by Goertzel in 1946 (Go46) and extended later by others, notably Alder (Al52), Abragam and Pound (Ab53) and Frauenfelder and Steffan (Fr68). The method has been used to study crystal structure problems, magnetic and electric interactions in insulators, a host of chemical compounds, hyperfine interactions in metals, structural defects, ion implantations, liquids, gases and biological materials. A rather extensive survey of recent works in the published literature is given by Rinneberg (Ri79).

Since its introduction, measurements have become more refined as the time resolving capabilities of detection apparatus have improved. Sodium iodide detectors are often used to detect the gamma emissions when decay energy information must be retained, but the relatively slow response of the scintillator material is responsible for limiting the minimum time resolution obtainable. In this thesis, the potential of using a deconvolution approach as part of a data analysis to improve the time resolution of the collected time interval distributions is investigated. This procedure involves using computer techniques to remove or "unfold" the influence the detection apparatus has on the observed time spectra. Forker and Rogers (Fo71) used a similar approach to partially remove the effects of finite time resolution using linear transform theory. That procedure works in principal but tends to amplify the spectral noise component, present due to counting statistics, to intolerable levels. The TDPAC effect is a second order effect and achieving good statistics (and hence a small noise component) can require very long count periods. In this study the Bayesian technique of spectral deconvolution, developed by Kennett et al. (Ke78a), has been employed as it is inherently more tolerent of signal noise.

The perturbation effect is seen as a time varying waveform in the time-interval spectra; the theoretical expression consisting of a sum of three cosine terms. Another aspect of this thesis looks at a least squares approach to calculating the frequency spectra of the measured data. This technique allows the data points to be weighted to accommodate a time dependent noise component (a fact of life in a TDPAC study).

This deconvolution approach has been used in a study of the extranuclear environment at the hafnium atom site in K_3HfF_7. A study of this material is of interest because it concerns the complex radical HfF_7^{3-}, the structure of which has been a point of controversy in the literature. In an earlier NMR study, Tarasov and Buslaev (Ta69) suggest the ZrF_7^{3-} ion in the structurally similar compound, K_3ZrF_7, may occupy one of two non-equivalent positions. Lowe and Prestwich (Lo77) performed a TDPAC study on K_3HfF_7 and found that their results can be fitted to a two site model for the hafnium atom at 77 K, while a one site model is sufficient to describe their room temperature observations. In the present study, this compound is examined in greater detail to determine the nature of the structural transition. This is done by recording the TDPAC spectra for a series of sample temperatures. At each step the form of the theoretical perturbation factor is fitted to the observations and the results interpreted in light of suggested structural models.

CHAPTER 2

THE THEORY OF PERTURBED ANGULAR CORRELATIONS

The "perturbed angular correlation" effect is the result of an interaction between the electromagnetic moments of a probe nucleus with extranuclear electromagnetic fields. A study of this effect can yield information about the host material in the immediate area of the probe nucleus. If the nuclear magnetic dipole moment is well known then an exact description of the local magnetic field is possible and likewise a knowledge of the nuclear electric quadrupole moment will enable a description of the electric field gradient. In this study use is made of a well documented excited state of ^{181}Hf to observe the electric field gradient at the hafnium site in K_3HfF_7.

This chapter introduces the equations required to describe the perturbed gamma-gamma angular correlation effect and to interpret the information available about the electric field gradient.

2.1 Angular Correlations

When an excited nucleus decays through an intermediate excited state with the release of two (or more) consecutive radiation quanta, the emission angle between these quanta is influenced by the angular momentum and parity changes taking place in the nucleus. The radiation types allowed for each transition are those which satisfy conservation of angular momentum laws and parity considerations. Of importance here is the decay of ^{181}Hf into ^{181}Ta through an intermediate state resulting in the emission of a gamma-gamma cascade. This gives rise to an unperturbed angular correlation component. However if the nucleus remains in the intermediate state long enough, as is the case with ^{181}Hf, the nuclear moments can interact with their environment causing the angular spin vector to precess. This alters the directional dependence of the gamma emissions and causes a perturbation in the observed angular correlation function.

2.2 The Unperturbed γ-γ Angular Correlation

The nuclear states shown in the gamma-gamma cascade in Figure 2-1 are eigenstates of the nuclear spin angular momentum with quantum numbers I_i, I and I_f for the initial, intermediate and final states respectively. The first transition changes the nuclear angular momentum by emitting a gamma photon with angular momentum $\hbar\vec{L}_1 = \hbar(\vec{I}_i - \vec{I})$. Since these are vector quantities, the necessary selection rules to conserve angular momentum for the two transitions are

$$/I_i - I/ \leq L_1 \leq I_i + I \qquad (2\text{-}1)$$

$$m_i = m + M_1$$

$$/I - I_f/ \leq L_2 \leq I + I_f$$

$$m = m_f + M_2$$

where m is the z-component of $\vec{I}$. The angular momentum, $\hbar L$, carried away with the electromagnetic radiation characterizes the multipolarity, 2^L, of the transition. An additional selection rule requires that the intrinsic spin of the photon be either parallel or anti-parallel to the direction of propagation because of the transverse nature of light waves.

The emission angle θ between the trajectories of the two gamma photons can be obtained by using two detectors (each with an energy window set about one of the gammas) and accepting only those events in which both detectors are activated within a resolving time of order one microsecond (figure 2-2). The resulting angular intensity distribution has been well studied and reviewed (Bi53, Pr62, Fr68). For the $I_i = 3/2^+$, $I = 5/2^+$, $I_f = 7/2^+$ transitions in ^{181}Ta the angular correlation function is

$$\overline{W}(\theta) = \sum_k A_k P_k(\cos\theta) \quad , \quad k=0,2,4 \qquad (2\text{-}2)$$

where $P_k(\cos\theta)$ is the Legendre polynomial of order k and A_k are the correlation factors. The latter depend only on the

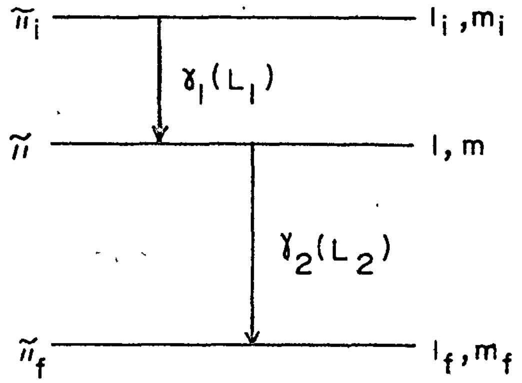

Figure 2-1. The parity ($\tilde{\pi}$) and angular momentum (magnitude I and z-component m) of the initial, intermediate and final states of a nucleus for a γ-γ cascade decay.

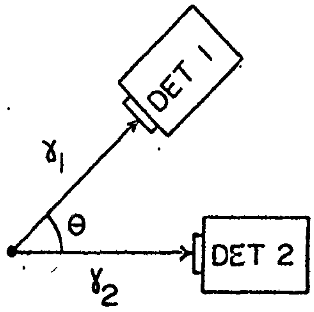

Figure 2-2. A two detector arrangement used to observe the angular γ-γ correlation.

angular momenta involved in the transitions and can be calculated using Clebsch-Gordan coefficients (Ro59). For practical experimental reasons considered in chapter 4.2, the $A_4P_4(\cos\theta)$ term is neglected here.

In this experiment the time of the second gamma emission is measured with respect to the first. Equation (2-2) therefore becomes

$$W(\theta,t) = \{ 1 + A_2P_2(\cos \theta) \} e^{-\lambda t} \qquad (2\text{-}3)$$

and is called the time-differential angular correlation where λ is the decay constant of the intermediate state (0.063 ns^{-1}).

2.3 The Perturbed Differential γ-γ Angular Correlation

The angular correlation of the gamma-gamma cascade will be altered if the orientation of the nuclear spin vector is changed while the nucleus is in the intermediate state. This perturbation is due to a coupling of the nuclear electromagnetic moments with the local electromagnetic fields and causes the alignment of the nuclear spins, ie. the population of the m sublevels, to be time-dependent (Ra63). This "time-differential perturbed angular correlation" (TDPAC) can be described by adding a time-dependent term to equation (2-3) giving

$$W(\theta,t) = \{ 1 + A_2G_2(t)P_2(\cos\theta) \} e^{-\lambda t}. \qquad (2\text{-}4)$$

The function $G_2(t)$ is called the perturbation factor and contains all of the information which can be obtained about the interaction of the nuclear spin with its environment. There is also a $G_4(t)$ component with the $A_4P_4(\cos\theta)$ term which can be neglected (in the case of ^{181}Hf).

In this study measurements are made at the two emission angles, 90 and 180 degrees. Expressing $P_2(\cos\theta)$ as $1/2(3\cos^2\theta - 1)$ in equation (2-4) gives

$$\begin{aligned} W(90,t) &= \{1 - \tfrac{1}{2}A_2G_2(t)\}e^{-\lambda t} \\ W(180,t) &= \{1 + A_2G_2(t)\}e^{-\lambda t} \end{aligned} \qquad (2\text{-}5)$$

Thus the angular distribution function $W(\theta,t)$ depends on:

a) the nuclear spin (I) of the intermediate state in the gamma-gamma cascade and the resulting interaction (magnetic dipole, electric quadrupole or both) and

b) whether the interaction is static or dynamic (ie. whether the extranuclear fields are static or dynamic).

This study examines an electric quadrupole moment interaction with an electric field gradient in a polycrystalline substance. Both static and dynamic components are observed and by using a powdered source the electric field gradient has a random orientation with respect to the gamma ray emission direction.

2.3.1 The Static Electric Quadrupole Interaction

The presence of an axially symmetric electric field gradient, $V_{zz} = d^2V/dz^2$, splits the I = 5/2 intermediate state into the twofold degenerate Zeeman levels m = $\pm 5/2$, m = $\pm 3/2$ and m = $\pm 1/2$ (see figure 2-3). Because the nuclei can flip amongst these levels, the perturbation factor contains three harmonics of the fundamental frequency, $\omega_1 = 3\omega_Q$, where

$$\omega_Q = -\frac{eQV_{zz}}{4I(2I-1)\hbar} = -\frac{eQV_{zz}}{40\hbar} \tag{2-6}$$

is called the quadrupole frequency and Q is the electric quadrupole moment. For a polycrystalline substance $G_2(t)$ is expressed as (Ri79)

$$G_2(t) = 1/35 \left\{7 + 13\cos(\omega_1 t) + 10\cos(2\omega_1 t) + 5\cos(3\omega_1 t)\right\} \tag{2-7}$$

Steffen and Frauenfelder (St64) show that a complete description of the non-axially symmetric electric field gradient can be made using only two parameters and Laplace's equation $V_{zz} + V_{yy} + V_{xx} = 0$. By convention $/V_{zz}/ \geq /V_{yy}/$

$\geq /V_{xx}/$ and an asymmetry parameter, η, is defined as

$$\eta = \frac{V_{xx} - V_{yy}}{V_{zz}} , \quad 0 \leq \eta \leq 1. \qquad (2\text{-}8)$$

Thus any electric field gradient can be characterized by its greatest component V_{zz} and a measure of the axial asymmetry η.

The Zeeman splitting of the magnetic m states is dependent on η (figure 2-4) and the three frequency components are no longer multiples of a fundamental frequency. The perturbation factor becomes

$$G_2(t) = a_0 + \sum_{n=1}^{3} a_n(\eta) \cos(\omega_n t) \qquad (2\text{-}9)$$

with both the amplitude and frequency of the three components dependent on η. The interaction Hamiltonian for the I = 5/2 spin state and solutions for $a_n(\eta)$ and $\omega_n(\eta)$ are given in Appendix I. Figure 2-5 shows the $G_2(t)$ function calculated for various values of η.

2.3.2 The Dynamic Electric Quadrupole Interaction

A continuously varying field gradient, in magnitude or direction, may eliminate the angular correlation completely. The randomly fluctuating field prevents the existence of a quantization axis for which the population of the m states may remain constant. Eventually all m states are equally populated and the directional correlation is

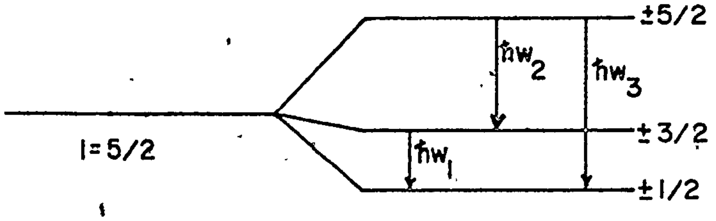

Figure 2-3. The I=5/2 state is split into the degenerate Zeeman levels.

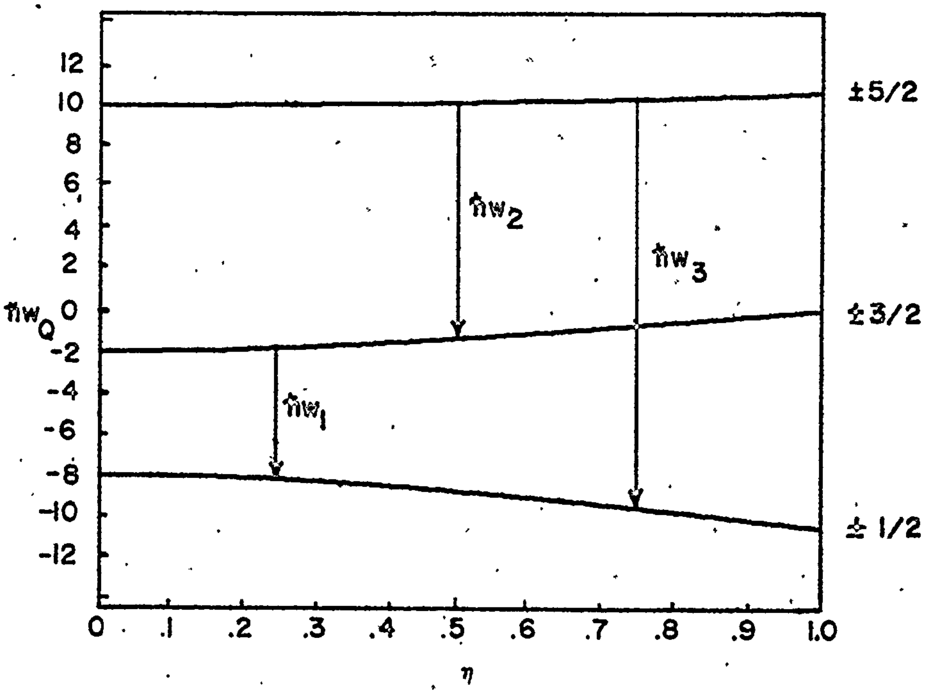

Figure 2-4 The splitting of the Zeeman levels as a function of η the asymmetry parameter.

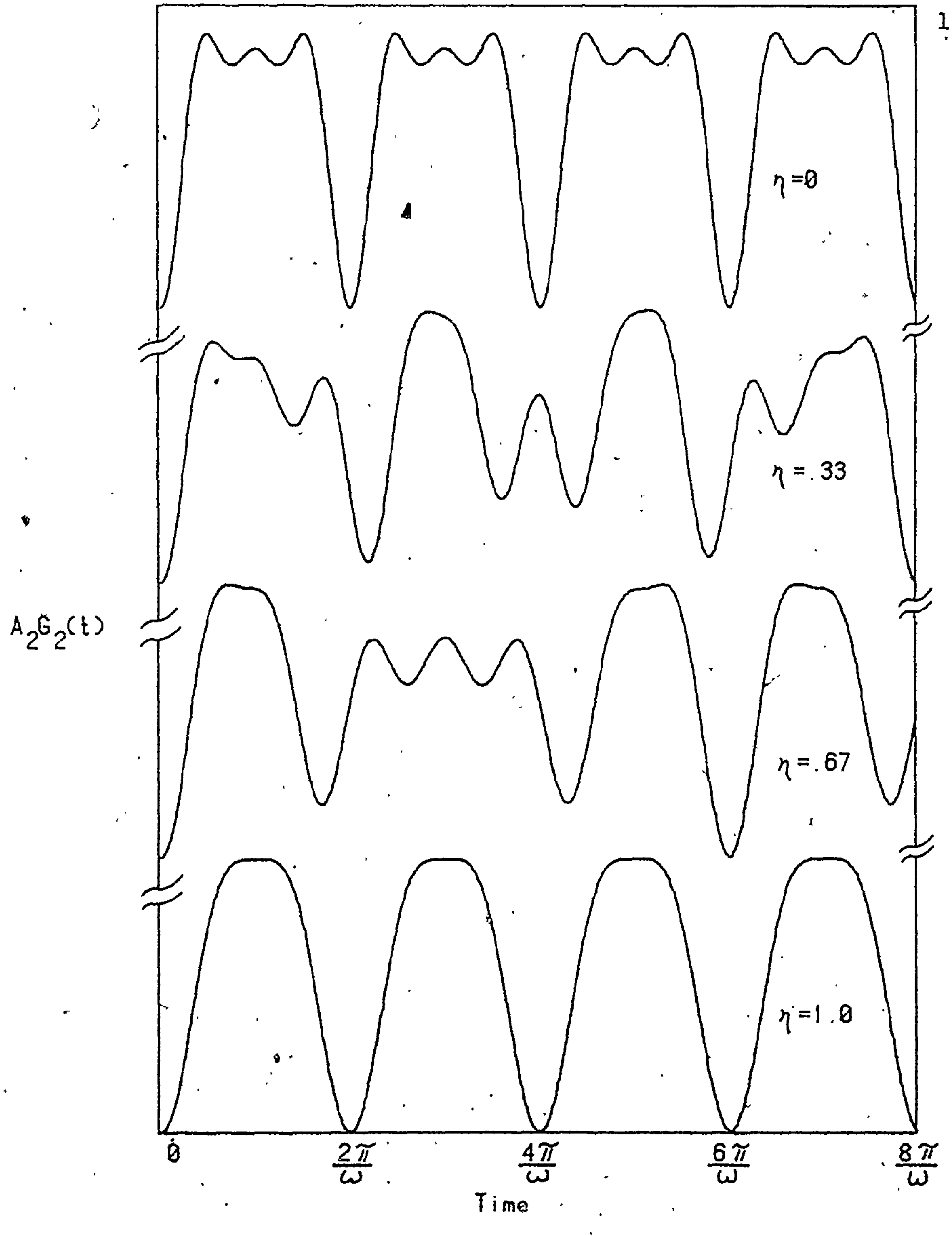

Figure 2-5. The perturbation factor, $G_2(t)$, for

η=0, .33, .67 and 1.0 with δ=0.

isotropic.

Steffen and Frauenfelder (St64a) discuss an exponential decay of $G_2(t)$ in time (often called the theory of Abragam and Pound) corresponding to a relaxation constant λ_k. Gerdau et al. (Ge73) found such an effect in room temperature studies of the similar compound $(NH_4)_3HfF_7$. Winkler (Wi73) gives a more detailed treatment of the matter and also suggests an exponential dependence.

The perturbation factor for a dynamic electric quadrupole interaction is therefore

$$G_2^d(T) = G_2^s(t)\, e^{-\lambda_k t} \tag{2-10}$$

where $G_2^s(t)$ results from the static interaction given in equation (2-9).

2.3.3 The Effect of a Finite Distribution in Vzz

Until now it has been assumed the electric field gradient has only one well defined value. Crystal impurities and imperfections or possibly atomic recoil following neutron irradiation will produce a range of V_{zz} values at the hafnium location causing a spread in the observed fundamental frequency. The shape of this distribution cannot be known precisely however a gaussian is considered here; it is both reasonable from a physical point of view and the simplest mathematically. Lorenztian and rectangular distributions have been suggested as possible candidates by other workers in separate studies. In a later chapter, an attempt is made to simulate the V_{zz} distribution and it is shown that the $G_2(t)$ function is not shape sensitive for the narrow spreads observed in this study.

The effect of the frequency spread can be calculated by evaluating a frequency averaged perturbation factor (2-9) (St64b)

$$G_2(t) = \frac{\int G_2(t)\ P(\omega)\ d\omega}{\int P(\omega)\ d\omega} \tag{2-11}$$

where $P(\omega)$ is the frequency distribution. For a gaussian spread characterized by δ, the relative width, the perturbation factor is

$$G_2(t) = a_0 + \sum_{n=1}^{3} a_n(\eta)\ e^{-1/2(\delta\omega_n t)^2} \cos(\omega_n t). \tag{2-12}$$

Examples of $G_2(t)$ for a selection of δ values with $\eta = 0$ are illustrated in figure 2-6.

The static electric quadrupole interaction can thusly be probed by making a least squares fit of ω_n, η and δ in (2-12) to the collected data.

As will be seen later, situations may exist in which the hafnium atoms populate one of two possible crystal sites. If each has a different electric field gradient, the

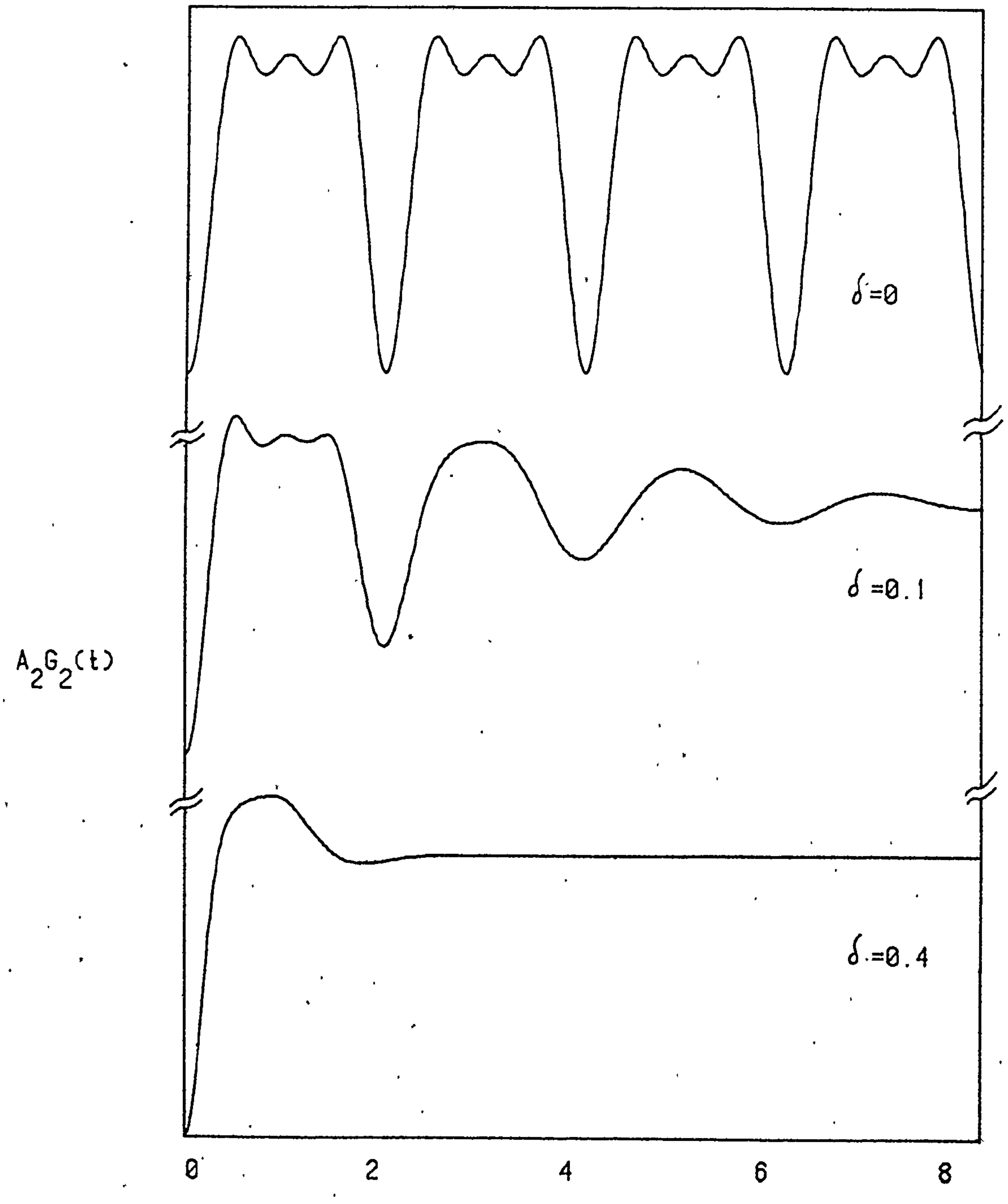

Figure 2-6. The perturbation factor, $G_2(t)$, for δ=0, 0.1 and 0.4 with η=0.

observed perturbation factor will be a weighted superposition of the two $G_2(t)$ functions, ie.

$$G_2(t) = p\, G_2^A(t) + (1-p)\, G_2^B(t) \qquad (2\text{-}13)$$

where p and 1-p are the population probabilities of site A and B respectively.

CHAPTER 3

DESCRIPTION OF THE EXPERIMENT

3.1 The Hafnium Source

^{181}Hf is widely used as a probe nucleus in perturbed angular correlation studies because the intermediate state in the gamma-gamma cascade has a number of desirable characteristics. These include

a) a large A_2 term resulting from the unperturbed angular correlation,

b) a large and well known electric quadrupole moment (+2.5 ± .2 barns),

c) a half life long enough to make time differential measurements (10.8 nsec, although longer would be better) and

d) cascade gamma emissions with pure (almost) multipolarities to keep the higher order terms $G_4(t)$,... small enough to be neglected.

The gamma spectrum and decay scheme for ^{181}Hf are given in figure 3-1.

Rinnberg (Ri79) lists the relevant properties of ^{181}Hf to TDPAC studies and compares them with 22 other nuclei which have been used in other studies reported in the literature.

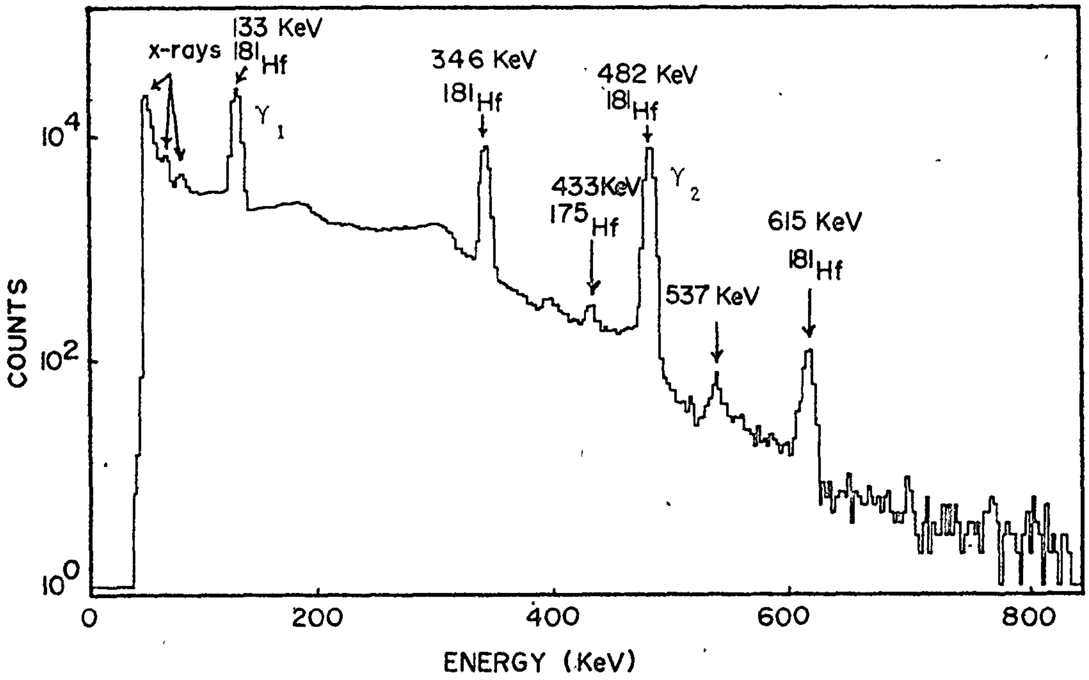

Figure 3-la. The gamma spectrum of ^{181}Hf obtained with a Ge(Li) detector.

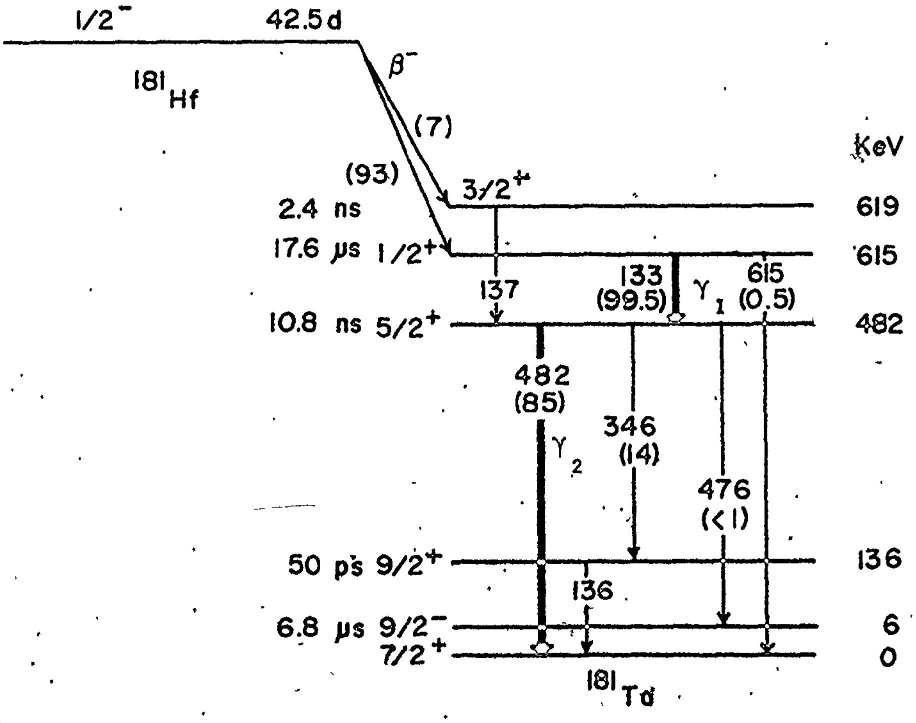

Figure 3-lb. The decay scheme of ^{181}Hf.

3.1.1 Sample Preparation

This work was not involved with the chemical preparation of the K_3HfF_7 source. Details have been reported elsewhere by Lowe (Lo76). Suffice it to say here that it was prepared as an inactive powder and sealed in a quartz vial. The purity was confirmed with an x-ray diffraction analysis. These x-ray photographs also showed the sample to be isomorphic with the similar compound K_3ZrF_7.

For this work the 6.8 mg sample was irradiated in the McMaster Nuclear Reactor in a neutron flux of 10^{13} n/s cm^2 for several hours giving a ^{181}Hf activity of approximately 10μCi. ^{181}Hf is the most abundant isotope of hafnium (35%) and has a capture cross section of 12.2 barns. Background activity from other isotopes was negligible after a short "cooling" period.

3.2 The Sample Chamber

The hafnium compound was placed in an evacuated aluminum structure. This allowed precise temperature control while maintaining a large counting solid angle (detector-source distance of 3.5 cm) as shown in figure 3-2. The source was placed on a copper cold finger which extended out of the evacuated chamber into a bath of ethyl alcohol. A Neslab CC-100f CryoCool unit cooled the alcohol to 180

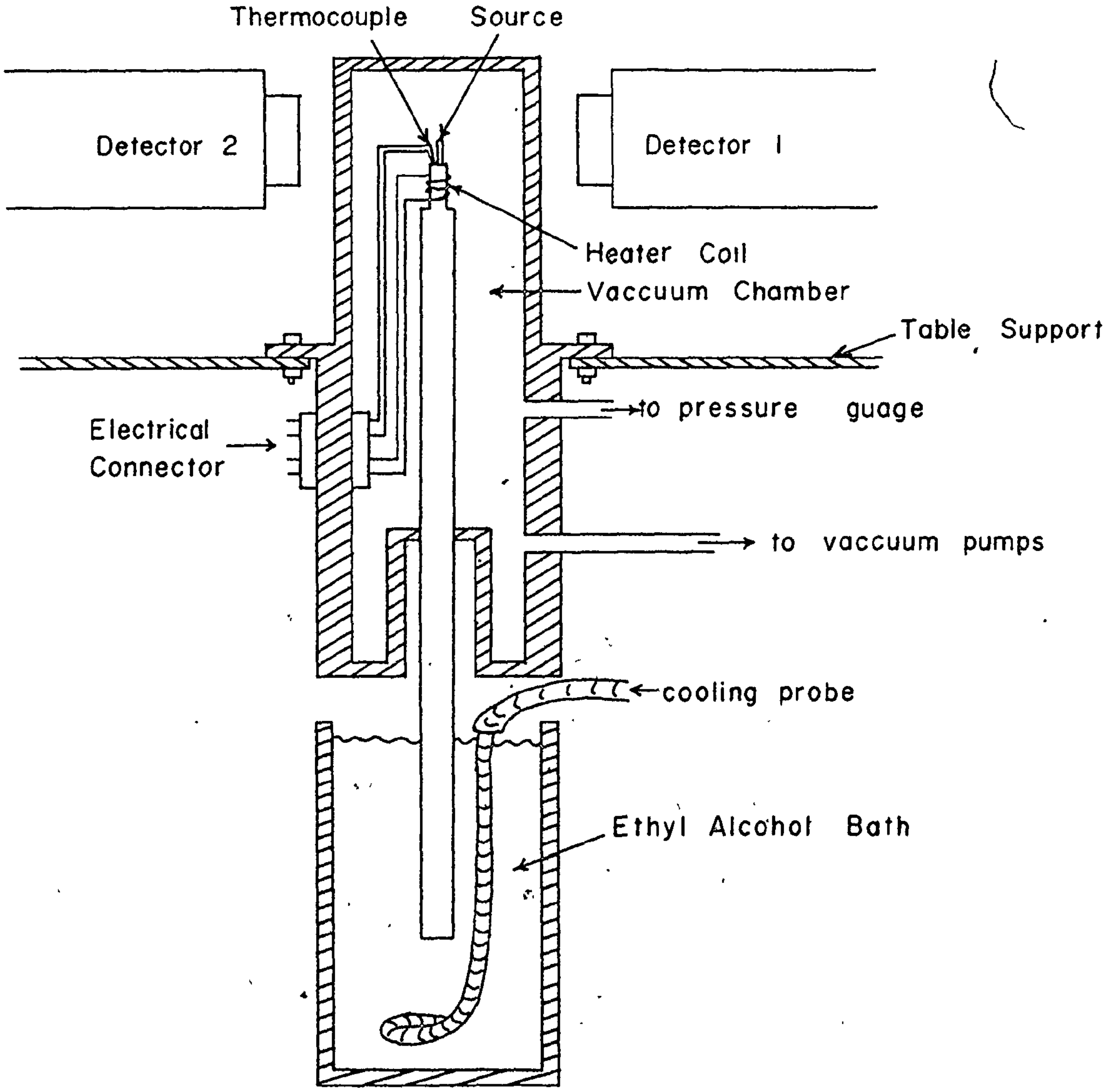

Figure. 3-2. Cut-away view of the sample chamber. (not drawn to scale)

Kelvin which in turn cooled the source to 210 K. For measurements below this temperature, the alcohol bath was replaced with a liquid nitrogen dewar (77 K). The temperature was monitored with a copper-constantan thermocouple placed in heat conducting silicon grease next to the source. A constantan heater coil was wrapped around the copper finger 5 mm below the source.

The chamber was evacuated to 5 x 10^{-8} torr with a mechanical piston pump and an oil diffusion pump in series. This kept the thermal conductivity of the air low to minimize heat transfer into the source. Air pressure was monitored with an ionization type pressure guage.

3.3 Sample Temperature Control

The heater coil current was controlled with a feedback circuit to keep the sample temperature constant. The current, proportional to the error signal (ie. the difference between the thermocouple reading and a preset reference voltage), was delivered to the coil by a programmable power supply. Coarse temperature adjustments were made by setting the reference voltage and fine adjustments were made with the feedback gain control. Figure 3-3 is a schematic of the temperature control circuit and figure 3-4 shows the circuit used to process the feedback signal.

A continuous record was made of the error signal

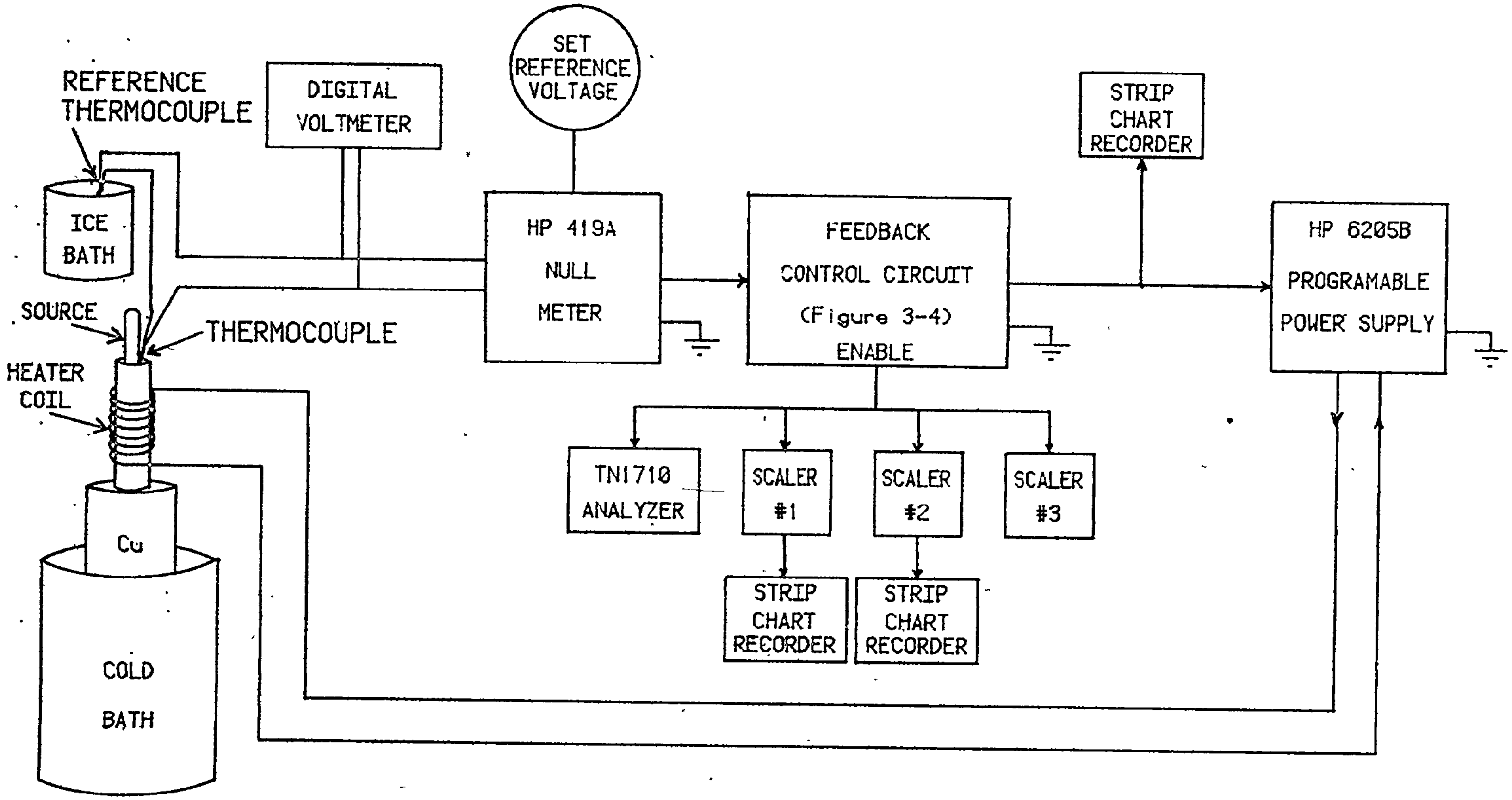

Figure 3-3. Schematic of the temperature control circuit

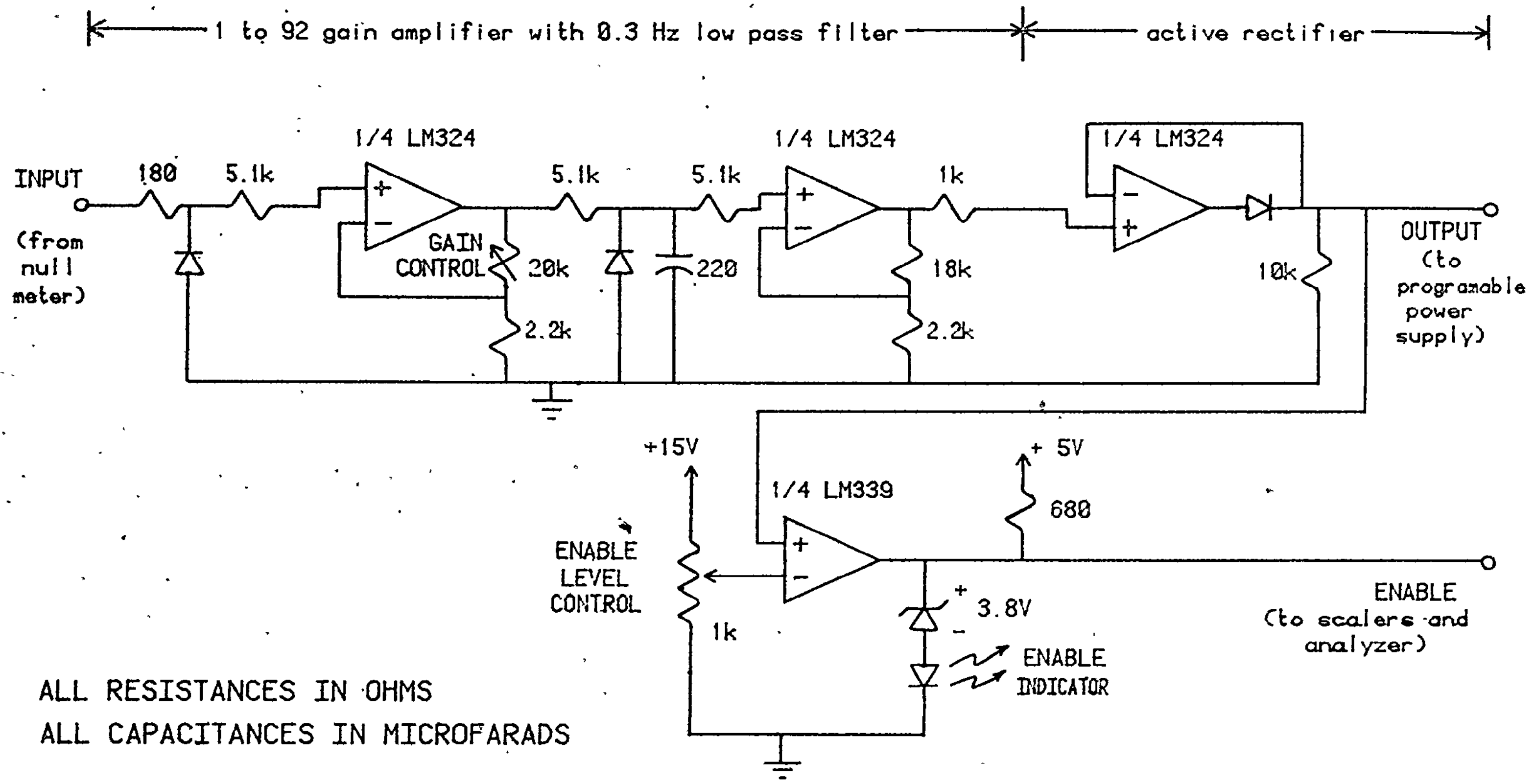

ALL RESISTANCES IN OHMS
ALL CAPACITANCES IN MICROFARADS

Figure 3-4. Schematic of the feedback control circuit.

magnitude on a strip chart recorder. This was related to the sample temperature variation and used to estimate the experimental uncertainty. The reference voltage was derived from a Hewlett Packard null meter using a mercury battery with high voltage stability. The absolute sample temperature was measured with a high impedance digital voltmeter directly across the thermocouple.

A large feedback gain in the control circuit is desirable for precise temperature control, however an excessively large gain will cause the system to become unstable. This problem was avoided by placing the heater coil physically close to the sample (and hence the thermocouple) to keep the thermal delay small and by adding a low pass filter to the feedback control circuit. The filter cutoff frequency (0.3 Hz) was decided upon by making a Bode plot of the system open loop gain and setting the gain low enough to ensure stability (Do74).

A voltage comparator was used to produce a logic signal when the heater current fell to a preset small value. This was used as an indicator that the liquid nitrogen (when used) level was low and disabled the counting scalers and analyser.

With this arrangement of a cold finger and heater, the K_3HfF_7 sample temperature was controled continuously from 130 to 320 K.

3.4 The Detectors : Time Resolution Considerations

The detection apparatus consisted of NaI scintillators and the associated photomultiplier tubes and detection electronics. The choice of detectors is made as a compromise between good time resolution and high detection efficiency. Germanium detectors have excellent energy resolution but are expensive, have low detection efficiencies and mediocre time resolution in the 5 to 50 ns range (eg. see MK68). Plastic scintillators have excellent time resolving capabilities due to a scintillation decay time of about 2 ns as compared to 250 ns for NaI, however the predominant gamma-ray interaction in the low Z number plastic is Compton scattering. The energy spectrum obtained consists of a very small photopeak superimposed on a large Compton continuum. Almost no energy information can be determined and so the 482, 346 and 133 keV gamma peaks emitted in the decay of ^{181}Hf can not be resolved. This would produce an undesirable large prompt peak in the time spectra background. Sodium iodide scintillators offer nanosecond timing and approximately 25 keV energy resolution.

Boulter (Bo71) showed experimentally that for minimum time resolution it is necessary to keep the scintillator crystal small in both the 133 and 482 keV energy regions.

This is to keep the number of internal reflections of scintillation photons in the crystal small to minimize the time dispersion of light collection. He experimentally verified theoretical expressions for NaI time resolution found in the literature (for example see Bi64, Do70, Wa70 and Si67) for crystal diameters up to one inch. His estimates for the best possible full width half maximum time resolution, Γ, in the region E >40 keV are given by the expression

$$\Gamma^2 = \frac{\tau_2}{pE} \left\{ 4 \ln(2)\tau_1 + 2\pi \frac{h(r+h)}{rv} \right\} \qquad (3\text{-}1)$$

where τ_1 and τ_2 represent the exponential rise time of the phototmultiplier tube (0.33 ns) and the scintillator decay time (220 ns) respectively, p the number of photoelectrons created per keV at an energy of E keV (10), v the velocity of light in NaI (c/1.77), and h and r the crystal height and radius.

For scintillator crystals much more than 1" in diameter, the dispersion in time of the collection of photocathode electrons by the first dynode becomes significant. Since a large portion of the cathode surface area is being illuminated, there is a finite spread in the cathode-dynode path length. A difference of 1/2 cm in 2 cm of electron acceleration distance will produce a spread of about 1 ns in a total of 4 ns transit time. This varies with photomultiplier tube design and operating voltage but can be more significant than equation (3-1). A further dispersion that is harder to estimate is introduced with large crystals due to electric field inhomogenities and edge effects in the tube.

In this study a 2" diameter by 1/2" thick NaI crystal on a RCA 8850 photomultiplier tube and a 2" diameter by 2" thick crystal with a RCA 8575 tube were used for the 133 and 482 keV detectors respectively. Both of these tubes are well suited for timing experiments because of low noise characteristics, high gain and a fast rise time of about 2 ns. The scintillator dimensions are such that each will introduce a similar time resolution limitation. The 133 keV detector was covered with a 0.8 mm cadmium absorber to filter the low energy x-rays and the 482 keV detectors were covered with 3 mm lead absorbers to reduce the intensity of the 133 keV gamma-rays. Each photomultiplier tube was wrapped in a μ-metal sheet to shield stray magnetic fields from interacting with accelerated photoelectrons in the tubes. The observed full width half maximum time resolution was 2.1 ns.

3.5 The Electronic Arrangement for Coincident Counting

A circuit configuration called a "fast-slow coincidence" circuit was used in this experiment. It consists of a slow coincidence detection arrangement between two detectors with microsecond time discrimination to isolate a decay in which both gammas in the cascade pair have been detected and a fast coincidence arrangement to measure the time interval between emissions with nanosecond discrimination. Figure 3-5 is a schematic of the three detector fast-slow circuit used in the experiment. The fast anode current pulses, indicating the initiation of a scintillating event, are converted into standard fast logic pulses with leading edge discriminators. The discriminator thresholds are set as low as possible above the noise level for minimum time resolution (Bo71). The discriminator pulses mark the start and stop events and are connected to the start and stop inputs of a time to amplitude converter (TAC). A TAC as a circuit which produces an analog pulse whose height is proportional to the start-stop time difference. This pulse is analyzed in a multichanel analyzer which accumulates a histogram of observed time intervals.

The slow coincidence circuit makes use of the slower dynode pulse whose amplitude is proportional to the gamma-ray energy. After amplification, the energy pulse from each detector is analyzed with a single channel analyzer. Simultaneous detection of a 133 and 482 keV gamma-photon corresponds to an "and" condition and is used to gate the fast coincidence side.

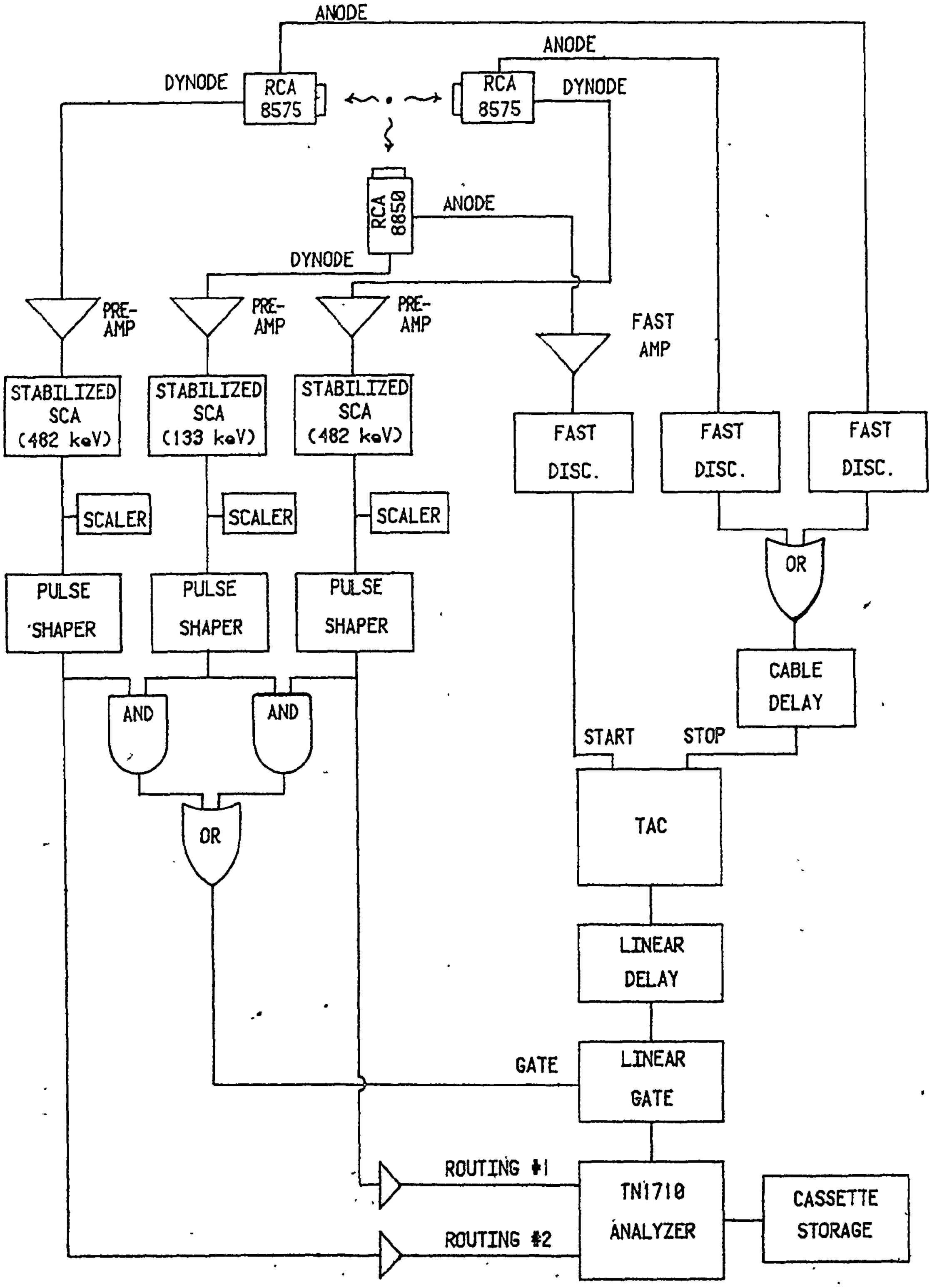

Figure 3-5. The three detector fast-slow coincidence circuit: The scalers and analyzer are also gated by an enable signal from the temperature control circuit.

Using three detectors instead of two doubles the effective counting solid angle. This allows simultaneous collection of spectra at both 90 and 180° emission angles. The start and stop signals were combined so that only one TAC, linear gate and pulse height analyzer were required, and then routed after digitization in the analyzer into separate memory halves with a routing signal. In this way, both spectra were subjected to identical electrical processing and suffered the same drifts and non-linearities allowing for a direct comparison when calculating the perturbation factor. Stabilized amplifiers, which have a self adjusting gain control, were used in the slow circuit to prevent gain drifts during the extended count periods.

The dead time of the TAC is controlled by the start pusle rate. In this experiment the 482 keV detector had the highest count rate and so was used as the stop signal. A cable delay of about 20 ns was inserted to shift the spectral time zero well above the analyzer threshold so that the chance coincidence count rate immediately before an event could be determined for background subtraction.

The total number of counts accepted by the single channel analyzers was recorded with a scaler for each detector. These were used to normalize the spectra before calculating the perturbation factor. Two spectra were collected simultaneously in a series of daily runs. The positions of the two stop detectors were exchanged each day so that when a series of runs were summed, any systematic differences would be common to both 90 and 180° data and tend to cancel allowing a direct calculation of the perturbation factor.

CHAPTER 4

INSTRUMENTAL EFFECTS INFLUENCING THE MEASURED PERTURBATION FACTOR

In addition to the statistical errors associated with the measured parameters in a DPAC study, several factors can lead to systematic errors. Karlsson (Ka71), Wagner and Forker (Wa69) and others have summarized and commented on some of these from time to time. This chapter examines effects that are relevant in the present context.

4.1 Finite Time Resolution : System Response

The effect of the finite time resolution of the experiment apparatus can be represented mathematically as the system impulse response function R(t) (see chapter 5.3). It can be measured directly by observing the positron decay of a ^{22}Na source with the fast-slow coincidence circuit. The emitted positron anihilates with an electron and produces two 511 keV gamma-photons 180° apart within 5 ps (due to finite source dimensions only) of each other. The SCA energy windows are set at 133 and 482 keV to correspond to experiment conditions so that only Compton scattered radiation in the scintillators within these windows is accepted. Figure 4-1 shows the resulting prompt peak (ie. response

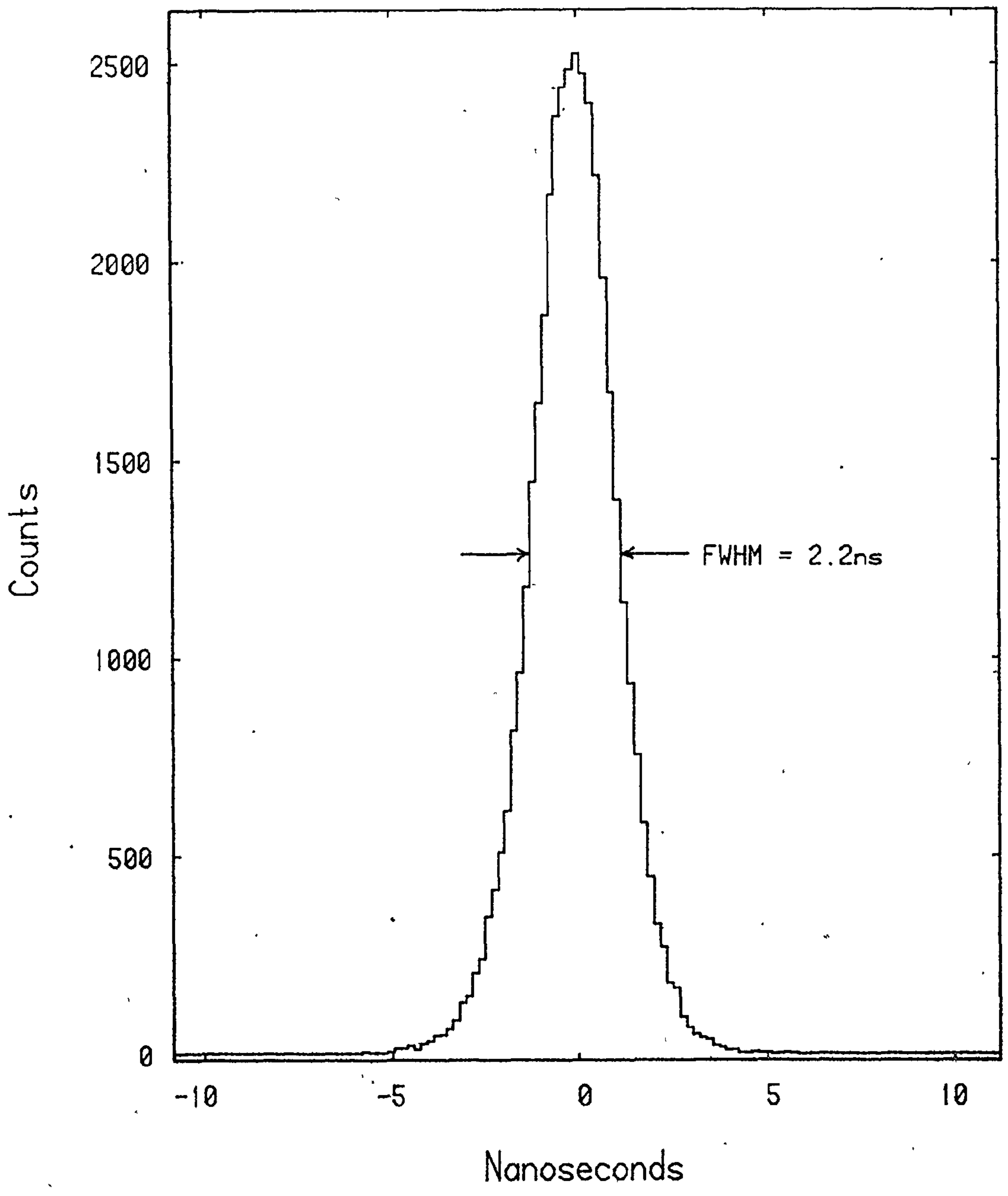

Figure 4-1. The system response function measured directly with a ^{22}Na source.

function) from which the full width half maximum time resolution (Γ) of 2.2 ns is measured. The peak closely approximates a gaussian curve although it has a slightly steeper slope on the right hand side reflecting slightly better resolution with the higher energy stop detector.

An indirect measurement of the response function can also be made from measured data. Referring to equation (2-5) the "true" data T(t) can be defined as

$$T(t) = W(180,t) + 2\ W(90,t) = C_o e^{-\lambda t} \qquad (4\text{-}2)$$

and the corresponding sum of the measured data after background subtraction is given by the convolution integral equation

$$\begin{aligned} M(t) &= \int_{-\infty}^{\infty} T(t-t')\ R(t')\ dt' \\ &= \text{[illegible]}\, e^{-\lambda t} \int_{-\infty}^{\infty} e^{\lambda t'}\ R(t')\ dt'. \end{aligned} \qquad (4\text{-}3)$$

Differentiating and solving for R(t) gives

$$R(t) = \frac{d}{dt} M(t) + \lambda M(t) \qquad (4\text{-}4)$$

from which the response function can be found by making a least squares estimate of λ for $t > 2$ (to avoid edge effects). Figure 4-2 shows a typical prompt peak obtained with equation (4-4). It suffers from a greater noise component than the direct method but offers a simple test of

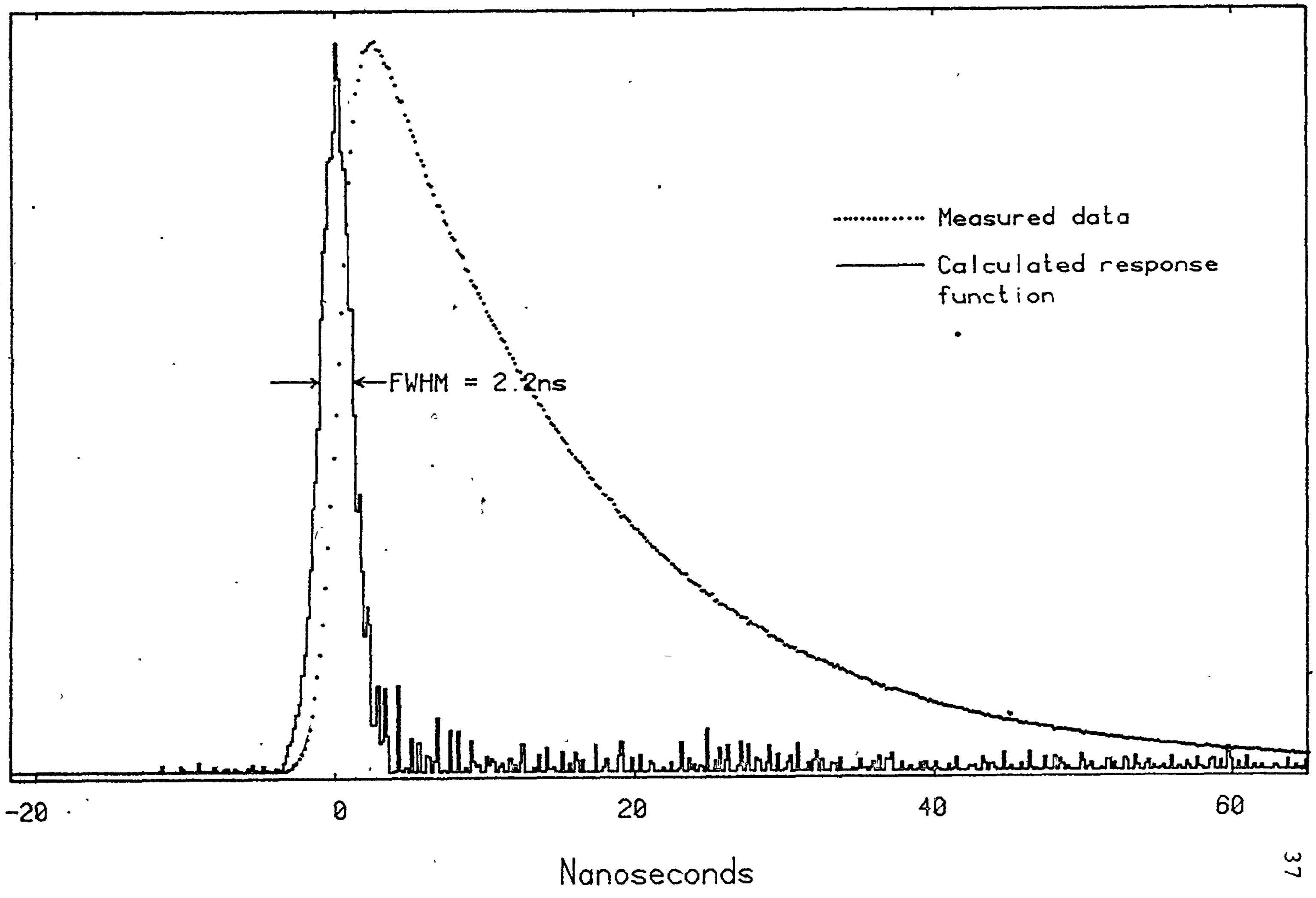

Figure 4-2. The system response function calculated indirectly from a measured data spectrum.

the actual resolution of a measured spectrum.

A gaussian response has the effect of attenuating high frequency components in the perturbation factor $G_2(t)$ by the term $e^{-\omega_n^2 \tau^2/2}$ where τ is the standard deviation of the gaussian curve given by 2.35 Γ. The appropriate correction must be made to the least squares fitted function, equation (2-12).

4.2 Finite Detector Solid Angle

The finite counting solid angle of the large NaI detectors has the effect of smearing the angular correlation dependence. Rose (Ro53) was first to report that this effect attenuates the magnitude of the correlation factor (A_k in equation 2-2) but not the form. The attenuation factor, $Q_k(i)$ for detector i, can be evaluated as

$$Q_k(i) = \frac{J_k(i)}{J_0(i)}$$

where

$$J_k = \int_0^{\gamma} P_k(\cos\theta)(1-e^{-rx(\beta)})\sin\beta \, d\beta \qquad (4-6)$$

and where $x(\beta)$ is the distance traversed by the radiation incident on the crystal at an angle β with the axis and γ is the maximum half angle subtended by the detector. Gardner (Ga69) showed that to a first order approximation the optimum value for the maximum half angle γ is about 45°, corresponding to a source-detector distance of 2.5 cm. Physical considerations restrict this to 3.5 cm in the present work.

The corrected angular correlation factors, A'_k, found by numerically evaluating equation (4-6) are shown in table 4-1 with the Legendre polynomials evaluated at the two emission angles 90 and 180°. As noted, A'_4 is much less than A'_2, justifying the approximation of neglecting the fourth order angular correlation factor in equation (2-2).

4.3 Time Scale Calibration

The absolute calibration of the time axis is required for an absolute measurement of the electric field gradient. This function was performed with a TAC calibrator circuit designed by Boulter (Bo70). The circuit produces start and stop pulses for the time to amplitude converter at intervals which are even multiples of a stable 100 MHz crystal clock period. Figure 4-3 shows a typical calibration spectrum. The peaks are 10 ns apart and a least squares fit of time to the peak centroid channel number gave the calibration as 0.1734 ± .0001 ns/channel. Inter-peak spacing was uniform to within 1% indicating an insignificant level of system non-linearity.

The timescale calibration was checked every few days during each series of runs and found to vary by less than 0.7%. This is considered negligible compared to statistical

ORDER (k)	A_k	$P_k(\cos 90^{\circ})$	$P_k(\cos 180^{\circ})$	Q_k	A'_k
0	1	1	1	1	1
2	-0.297	-1/2	1	.62	-.18
4	-0.069	3/8	1	.17	-.01

Table 4-1. The angular correlation factors A_k corrected for finite detector width are shown with the Legendre polynomials evaluated at emission angles of 90 and 180°.

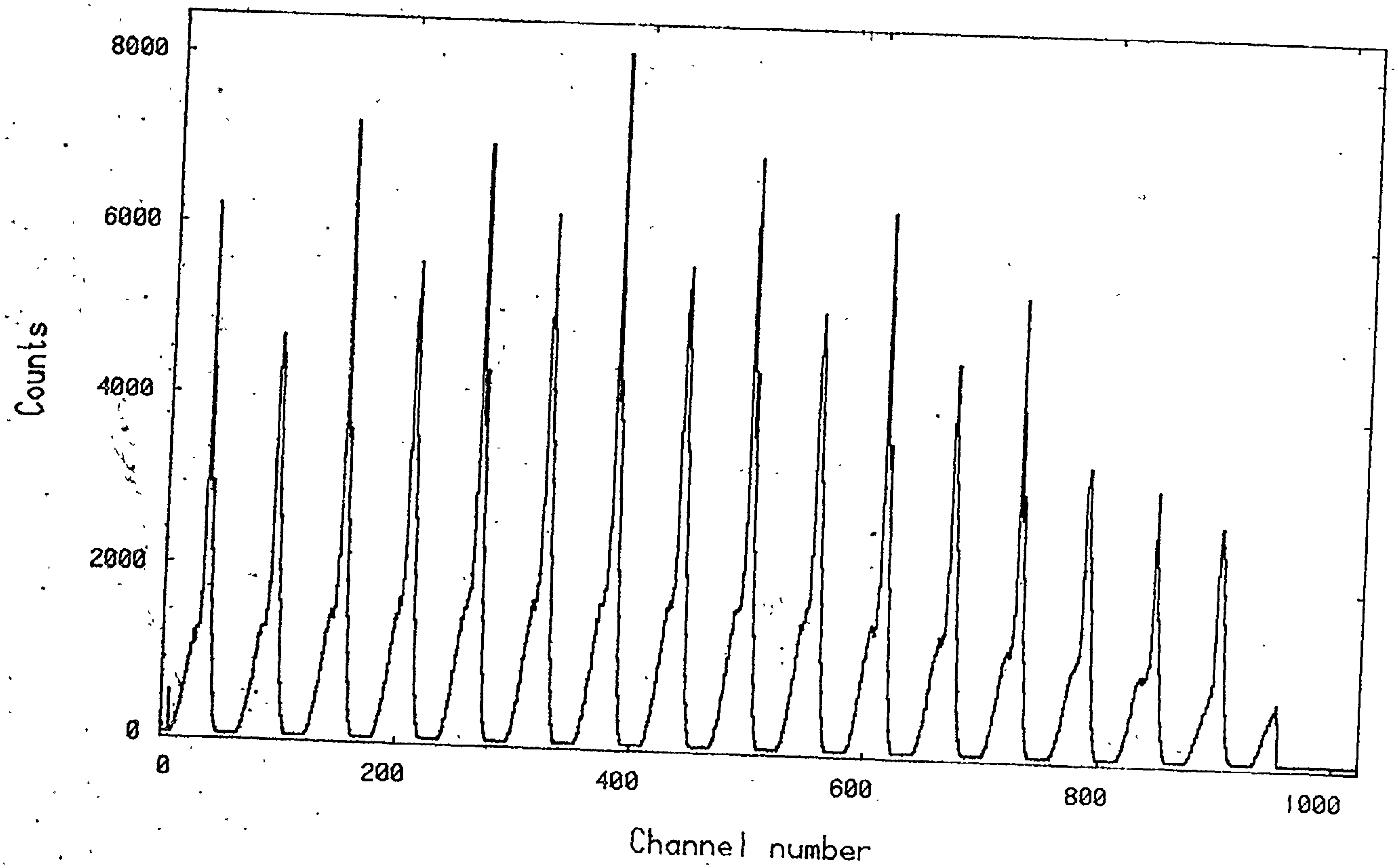

Figure 4-3. Time scale calibration spectrum.

errors in the measured data.

4.4 Accidental Coincidences (Background)

The desired coincidence spectrum in a TDPAC study is superimposed on a background of accidental coincidences. If this background count rate is low, it has the form $\exp(-\lambda_b t)$ where λ_b is the probability per unit time of a chance coincidence. Lowe (Lo76) showed that in general the correlated and chance distributions are not independent but interact to suppress the background level corresponding to time intervals greater than those associated with the correlated event. This comes about because the TAC can respond to only one stop signal per start event.

The shape of the background before and after a prompt correlated start-stop event, $N_1(t)$ and $N_2(t)$, can be given as

$$\begin{aligned} N_1(t) &= N_1 e^{-Rt} && t<t_p \\ N_2(t) &= N_2 e^{-Rt} = (1-F)N_1 e^{-Rt} && t>t_p \end{aligned} \tag{4-7}$$

where F is the probability that a correlated start-stop event has been detected and R is the stop event count rate. In a TDPAC study the correlated events are distributed in time and F becomes an integral expression. The resulting observed time-interval distribution is the sum of C(t), the correlated time-interval distribution, weighted by the probability that a background event has not been detected and $U(t)$, the uncorrelated distribution, weighted by the probability that a correlated event has not been detected. ie.

$$N(t) = C(t) \left\{ 1 - G(t) \right\} + U(t) \left\{ 1 - F(t) \right\} \qquad (4\text{-}8)$$

where

$$F(t) = \int_0^t \frac{C(t)dt}{N_s}$$

$$G(t) = \int_0^t \frac{U(t)dt}{N_s}$$

$$U(t) = N_1 e^{-Rt} = N_s R e^{-Rt}$$

and N_s = start rate. An iterative solution for the correlated time-interval distribution, tested experimentally by Lowe, is

$$C_{j+1}(t) = N(t)e^{-Rt} - N_1 \left\{ 1 - \frac{N_1 - N_2}{N_1} \frac{\int_0^t C_j(t)dt}{\int_0^\infty C_j(t)dt} \right\} \qquad (4\text{-}9)$$

where N_1 and N_2 can be determined from the background with equations (4-7) before and well after the correlated event respectively. Lowe showed that one iteration of (4-9) is usually sufficient and the result is very insensitive to the initial estimate of $C(t)$. It was approximated as $N(t)$ in this study.

CHAPTER 5

DATA ANALYSIS

The ultimate aim of this study is to make an accurate estimate of the parameters describing the electric field gradient. This is done by making a least squares fit of the parameters in equations (2-10), (2-12) and (2-13) to measured data. An effort put into a pretreatment of the observed information (before the least squares fit) can be rewarded with a reduction in the number of free parameters fitted. Fewer parameters means a reduced chance of an erroneous fit and greater confidence in the fitted values. Several authors have used this approach before to varying degrees. Gardner and Prestwich (Ga70) and Gerdau et al. (Ge69) have made Fourier Transform analyses of perturbation factors. In both cases the results were used only as a first estimate of the frequency components in a least squares fit. Forker and Rogers (Fo71) discussed limitations in the usefulness of the Fourier method and used a linear inverse transform approach to partially remove the effect of finite time resolution on the time spectra. Reddy (Re70) discussed the interpretation of results from spectral density measurements from a more theoretical standpoint.

In this study the data analysis process has been divided into four steps:

a) extraction of the perturbation factor $G_2(t)$,

b) a Fourier analysis to determine the frequency components in $G_2(t)$,

c) a deconvolution analysis to remove the response function of the equipment used in the experiment and

d) a least squares fitting of the $G_2(t)$ function to estimate the parameters.

This section provides a short description of some techniques used. The results are presented in the following chapter.

5.1 The Fourier Transform

A Fourier transform is a linear transformation from one domain (often the time domain) to another (often the frequency domain) or vice versa. It has a very general application, however in this work we are interested in the frequency spectrum of a time varying waveform. The transformation can be defined as

$$F(s) = \int_{-\infty}^{\infty} f(x) e^{-i2\pi xs}\, dx$$

$$f(x) = \int_{-\infty}^{\infty} F(s) e^{i2\pi xs}\, ds \qquad (5-1)$$

where x and s are conjugate variables in the two domains. A useful quantity is the power spectrum $/F(s)/^2$ as it is a measure of the energy associated with each frequency component. A practical and intuitive description of the Fourier transform with reference to applications is given by Bracewell (Br78) and others.

In most computer applications the above integrals are not solved analytically but an efficient numerical routine, often referred to as the "discrete fast Fourier transform", is used. Details on it can be found in any text on the subject. Figure 5-1 is an illustration of the transform of a simple waveform calculated with a discrete fast Fourier transform routine.

5.2 An Alternative Fourier Transform Using a Weighted Least Squares Approach

In most applications data to be transformed contains some sort of statistical noise. If the noise component is constant across the sample set the discrete transform does as well as is possible under the noise conditions. There is no (practical) way of weighting data to accommodate a noise component that varies. The following section describes an alternative transform that will produce the frequency power spectrum with an arbitrarily weighted emphasis.

Consider $S_k(t)$ as an approximation of some function f(t) over the space $-T/2 \leq t \leq T/2$ where

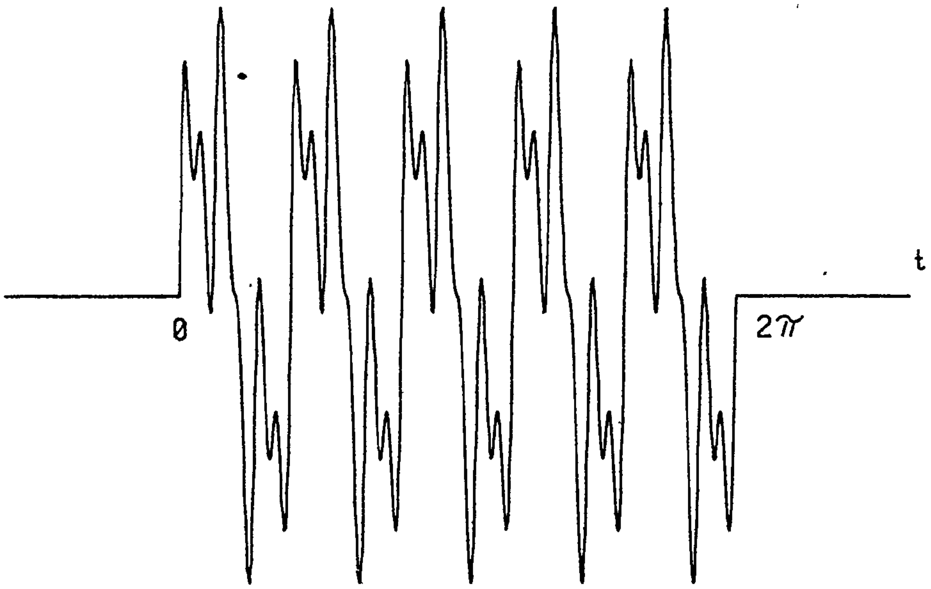

a) $f(t) = 1 \sin(5t) + .75 \sin(10t) + .5 \sin(20t)$
for $0 < t < 2\pi$.

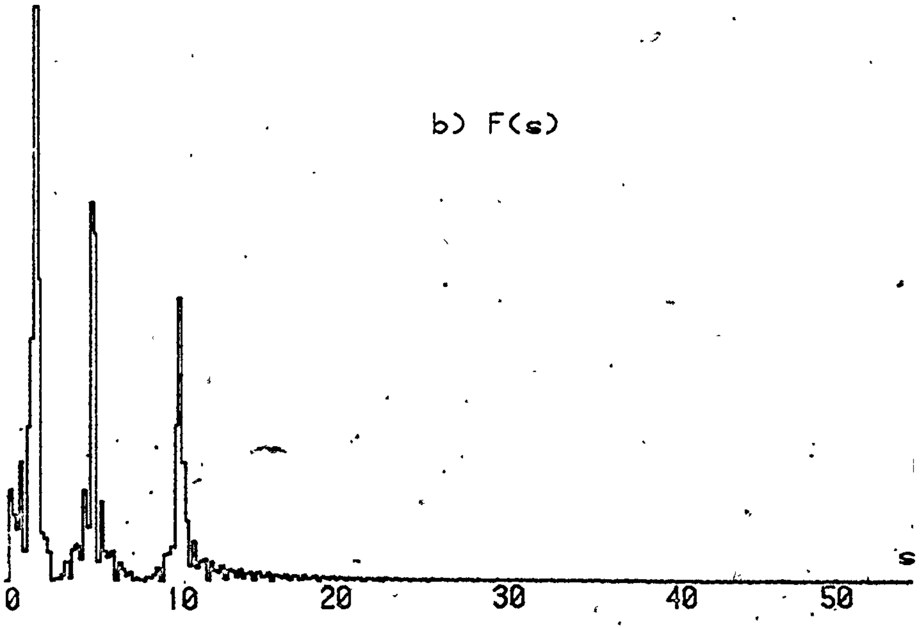

Figure 5-1. a) A waveform in the time domain and
b) its transform in the frequency domain.

$$S_k(t) = a_0 + \sum_{n=1}^{k} (a_n \cos n\omega t + b_n \sin n\omega t). \qquad (5\text{-}2)$$

$S_k(t)$ is then a finite Fourier series with (2k+1) terms. The weighted mean error is given by

$$E_k = \frac{1}{T} \int_{-T/2}^{T/2} \frac{1}{\sigma^2(t)} \left\{ f(t) - S_k(t) \right\}^2 dt$$

$$(5\text{-}3)$$

$$= \frac{1}{T} \int_{-T/2}^{T/2} \frac{1}{\sigma^2(t)} \left\{ f(t) - a_0 - \sum_{n=1}^{k} a_n \cos(n\omega t) - \sum_{n=1}^{k} b_n \sin(n\omega t) \right\}^2 dt$$

where $1/\sigma^2(t)$ is the assigned weighting. In the simpler case where $\sigma(t)$ is constant in time, minimizing E_k by making a least squares fit of a_0 and a_n to the data produces the result (Hs70)

$$\frac{dE_k}{da_0} = 0 = a_0 - \frac{2}{T} \int_{-T/2}^{T/2} f(t)\, dt$$

$$\frac{dE_k}{da_n} = 0 = a_n - \frac{2}{T} \int_{-T/2}^{T/2} f(t) \sum_{n=1}^{k} \cos(n\omega t)\, dt \qquad (5\text{-}4)$$

$$\frac{dE_k}{db_n} = 0 = b_n - \frac{2}{T} \int_{-T/2}^{T/2} f(t) \sum_{n=1}^{k} \sin(n\omega t)\, dt.$$

If S_k is a simple series approximation with only one harmonic term then the a_n and b_n terms are recognized as being

Fourier coefficients. In this way the transform can be calculated by making a least squares fit of a_0, a_1 and b_1 to f(t) as a function of ω. The weighted transform of a discrete data set with arbitrary weighting σ_i is calculated by differentiating equation (5-3) and calculating the power spectrum as $P(\omega) = a_1^2(\omega) + b_1^2(\omega)$. Figure 5-2 shows a comparison of the discrete fast Fourier and weighted Fourier power spectra. The latter is more tolerant of spectral noise because the higher frequency components are filtered in proportion to the statistical uncertainty. Frequency resolution can become very poor if σ_i^2 covers a large dynamic range. In the present work the minimum weighting was restricted to 1% of the maximum.

5.3 The Convolution Integral

The convolution integral is related to the Fourier transform as it is the operation in the time domain analogous to multiplication in the frequency domain. Using the notation of Bracewell it can be defined as

$$M(x) \doteq \int_{-\infty}^{\infty} f(u)g(x-u)du = f * g \qquad (5\text{-}5)$$

in the time domain and as

$$M(s) = F(s)\ G(s) \qquad (5\text{-}6)$$

in the frequency domain. It is the mathematical description

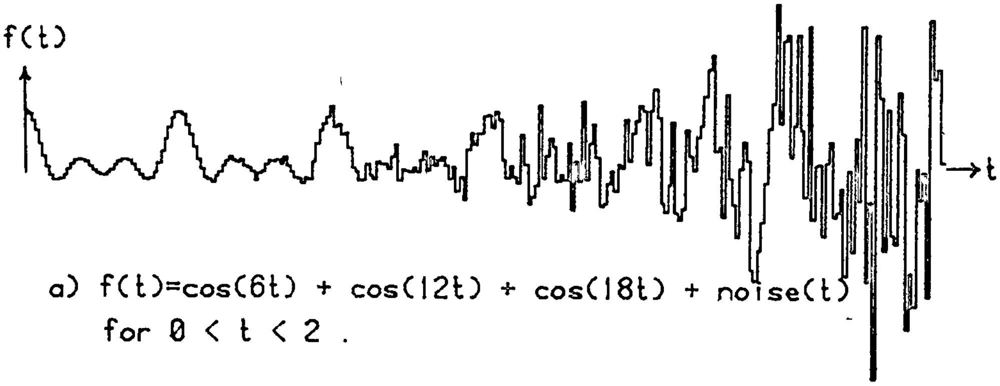

a) f(t)=cos(6t) + cos(12t) + cos(18t) + noise(t)
for 0 < t < 2 .

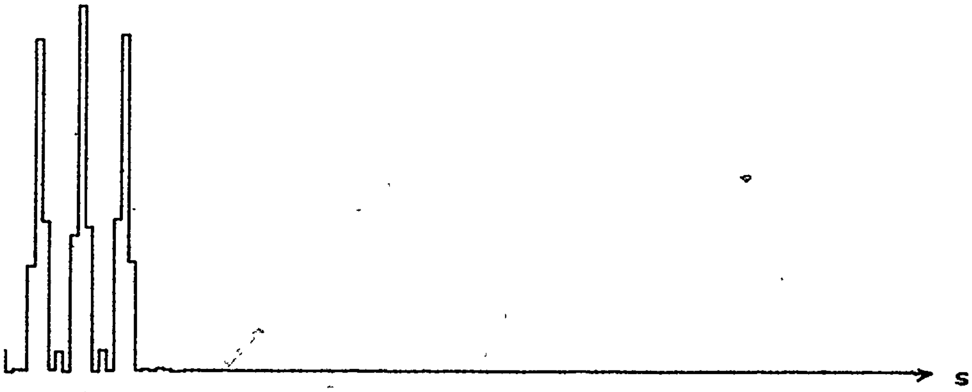

b) The weighted least squares power transform of f(t).

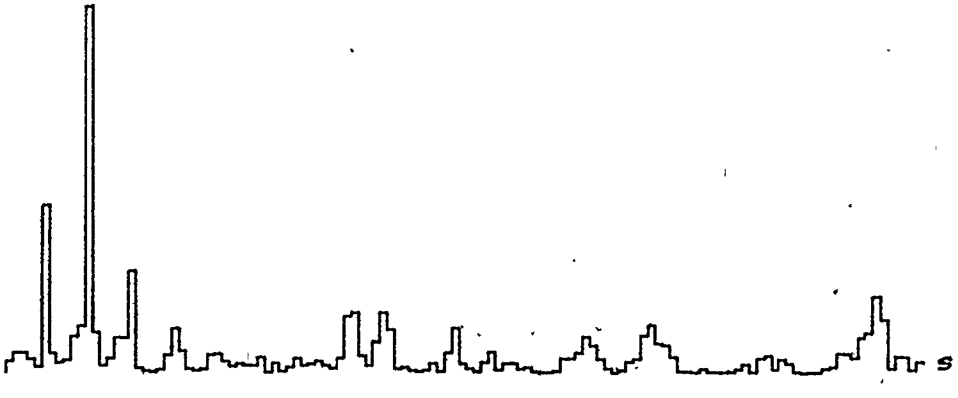

c) The discrete fast Fourier power transform of f(t).

Figure 5-2. A comparison of the weighted least squares Fourier transform with the discrete fast Fourier method for a data set with a time dependant noise component.

of "folding" one function through another. For example, if g(x) represents the true perturbation factor T(x) (that which would be measured with ideal equipment and perfect time resolution) and f(u) describes the response characteristics of the instrumentation R(x) then the measured spectrum can be expressed as

$$M(x) = \int_{-\infty}^{\infty} R(x-x')T(x)dx' + N(x) \qquad (5\text{-}7)$$

$$= \int_{-\infty}^{\infty} R(x')T(x-x')dx' + N(x)$$

and $$M(s) = R(s)\ T(s) + N(s). \qquad (5\text{-}8)$$

N(x) is the noise component normally due to counting statistics. Figure 5-3 shows a simulation of the perturbation factor combined with an exponential curve as described by equations (2-5) and (2-9). The simulation of the "measured" spectrum is obtained by letting R(x) be a gaussian curve with a width equal to the time resolution of the apparatus. In addition to adding a noise component, a more realistic simulation can be generated by letting R(x) be the measured system response to an impulse stimulus which may not be gaussian.

5.4 Deconvolution Techniques

The intent of a deconvolution analysis is to remove the system response function from measured data to make an

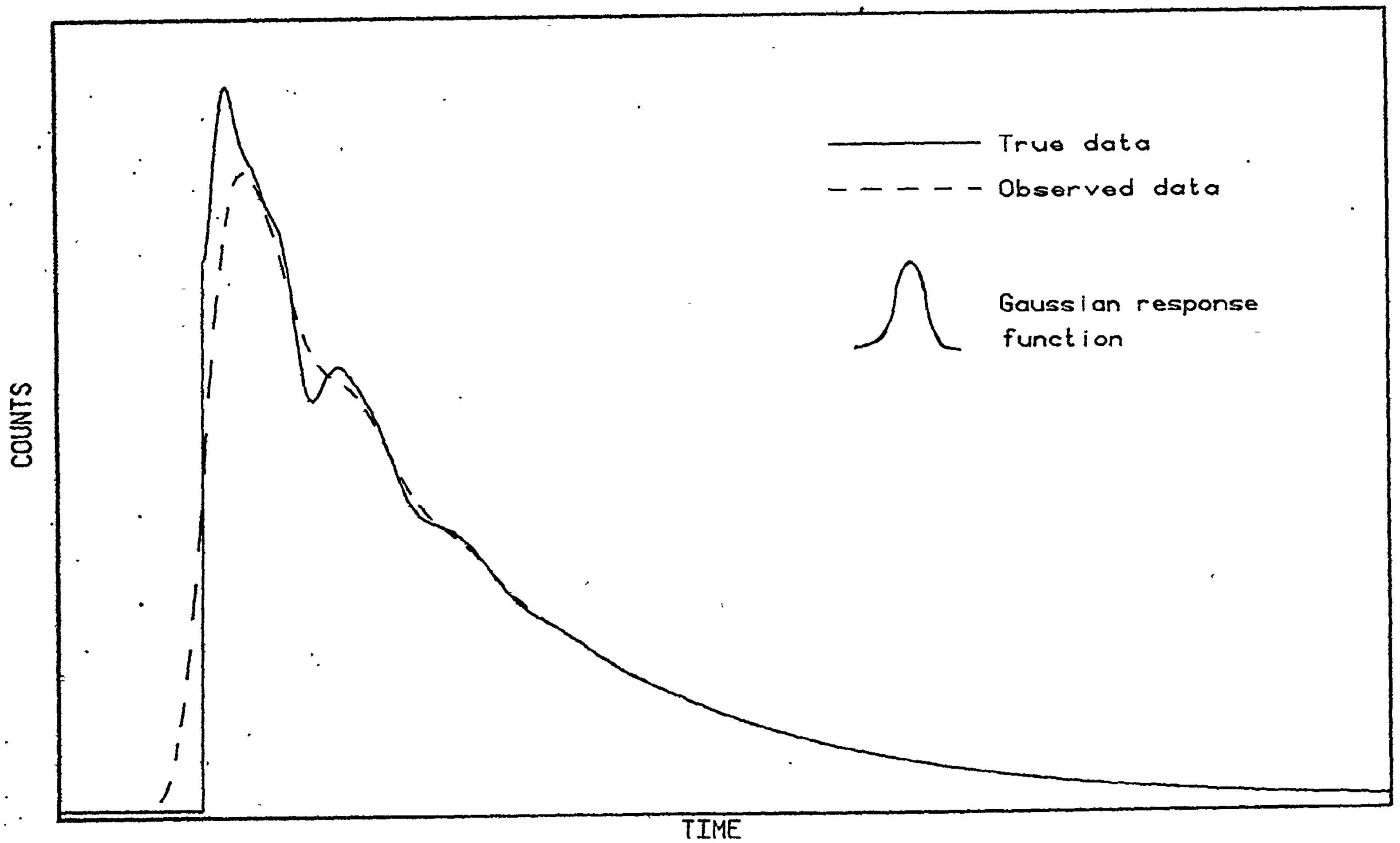

Figure 5-3. Simulation of an observed data spectrum by convolving the true data with a gaussian response function.

estimate T'(x) of the "true" information. This is the inverse operation to convolution and in the frequency domain is expressed as

$$T'(s) = \frac{M(s)}{R(s)} + \frac{N(s)}{R(s)} = T(s) + \frac{N(s)}{R(s)} \qquad (5\text{-}9)$$

In principal this expression can be evaluated uniquely for T'(x) however the noise term N(s)/R(s) leads to a variance in T'(s) proportional to $1/R^2(s)$. For a gaussian response function of the form e^{-x^2} with the transform e^{-s^2} the noise contribution is $e^{2s^2}N(s)$ which becomes excessively large very quickly with s. This is the limiting factor in the usefulness [illegible] the linear approach.

An alternative non-linear technique has been reported by Kennett et al. (Ke78a, Ke78b, Ke78c) and applied to the analysis of gamma-ray spectra. It is an iterative approach based on Bayes' theorem dealing with probabilities and as such assures positivity of solution. Both techniques conserve area but while the linear result may contain random large negative values and hence a large positive noise component, the Bayesian alternative is always positive, restricting noise growth. Suppressing noise growth is important in this study where the perturbation factor is a second order effect and good counting statistics require very long count periods.

Following the matrix notation of Kennett et al., each iteration can be expressed as

$$T_i^{(n+1)} = T_i^{(n)} \sum_k \frac{R_{k,i}\ M_k}{\sum_j R_{k,j}\ T_j^{(n)}} \qquad (5\text{-}10)$$

which is easily adapted into a computer routine. The first estimate of T_i is taken as the measured data M(x) and with each iteration $T_i^{(n)}$ more closely approximates the "true" information. For comparison with the linear deconvolution technique, equation (5-10) can be re-written as

$$T^{(n+1)}(x) = T^{(n)}(x)\ R(x) \circledast \frac{M(x)}{R(x) * T^{(n)}(x)} \qquad (5\text{-}11)$$

in the time domain where * and ⊛ represent convolution and correlation operations respectively. Kennett et al. show in (Ke78a) that solutions to equation (5-10) will converge about the "true" data and in (Ke78b) discuss noise growth.

As an illustration, the dashed curve of figure 5-3 has been deconvolved using equation (5-10) and shown in figure 5-4. The perturbation factor becomes more clearly resolved as the effective time resolution improves with iterations. The merits of this are self evident and become increasingly important when high frequency components are present. In addition, the spectrum slope at time zero becomes steeper allowing for a more precise estimate of the

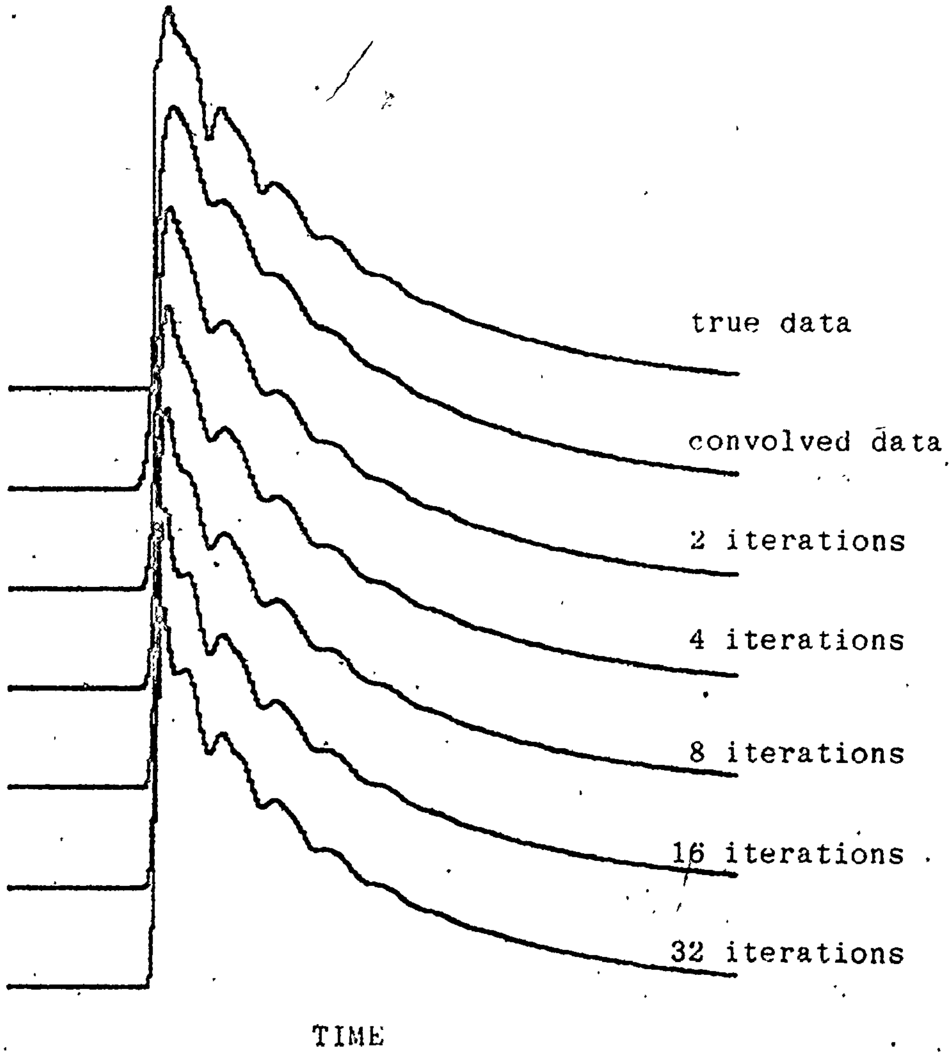

Figure 5-4. Bayesian deconvolution of a simulated spectrum.

true time zero channel. The benefit of this is discussed in the next section.

The only distortion is seen as an oscillation near t=0. This may have to be tolerated as it appears to be a consequence of the improved but still finite frequency spectrum. A similar effect can be generated by filtering a simulated "true" data spectrum with a sinc function thereby removing the upper half of the frequency components.

Figure 5-5 shows a similar spectrum deconvolved using the linear inverse transform technique given in equation (5-9). The larger noise component N(s)/R(s) quickly masks the perturbation factor restricting the usefulness of this method. No further use was made of the linear inverse transform.

5.4.1 Deconvolution for the Time Zero Channel

It is common practice in TDPAC studies to estimate the time zero position as the channel with one half of the maximum exponential height. This channel is used as a reference for aligning the spectra collected at the two emission angles. Due to the finite equipment time resolution this approximation can have a significant error if the perturbation factor contains sufficient detail near t=0.

The usefulness of deconvolving data before estimating the time zero channel was studied by simulating spectra

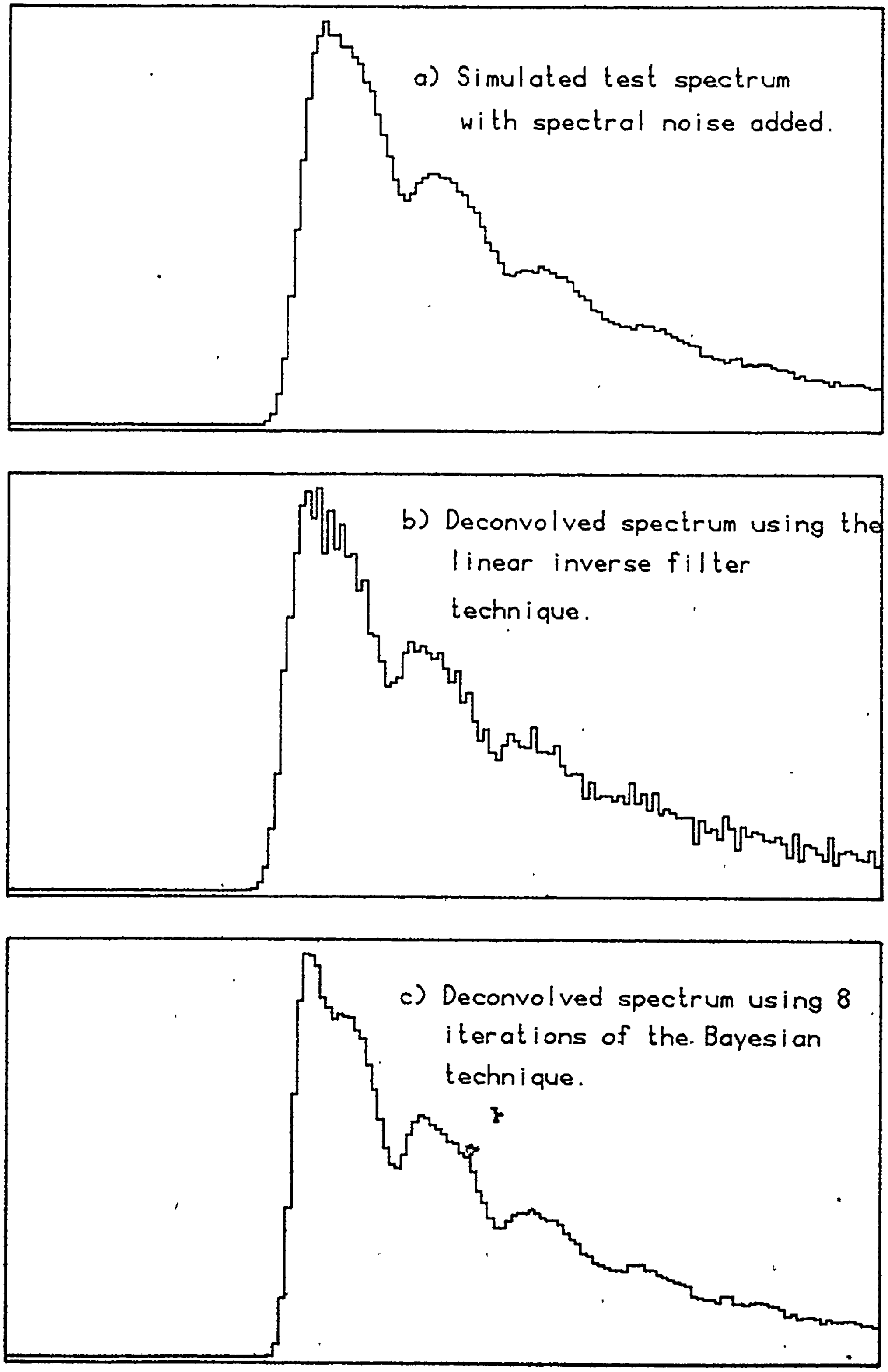

Figure 5-5. Comparison of the linear inverse filter deconvolution with the Bayesian approach.

for both emission angles and calculating the difference in the half maximum channels as a function of the Bayesian iteration index. This alignment error is plotted in figure 5-6 as a function of the time resolution τ, exponential decay constant λ, and $G_2(t)$ fundamental frequency ω_1. All but τ are expressed in terms of τ for generality which was chosen as 6 channels to coincide with the experiment time resolution and to give sufficient detail near time zero. The ratio λ/τ was varied from 1/4 to 1/1024, covering decay times of all nuclei popular in TDPAC studies.

In all cases the error has been reduced substantially; the best improvement occurring when $G_2(t)$ has a low fundamental frequency and the decay constant is small (long half life). The simulation closest to actual experiment parameters showed an error reduction from 1.0 to 0.2 channels. The alignment error in real data was studied by deconvolving the fifteen pairs of collected spectra and comparing the half maximum channels before and after the deconvolution process. In agreement with the simulation study, all cases showed an error of one channel.

This result suggested that after aligning the half maximum points an additional one channel shift of the 180° spectrum towards increasing time was required. This is a small correction (about 1/6 τ) but has a significant effect near t=0; figure 5-7 shows this shift is almost completely

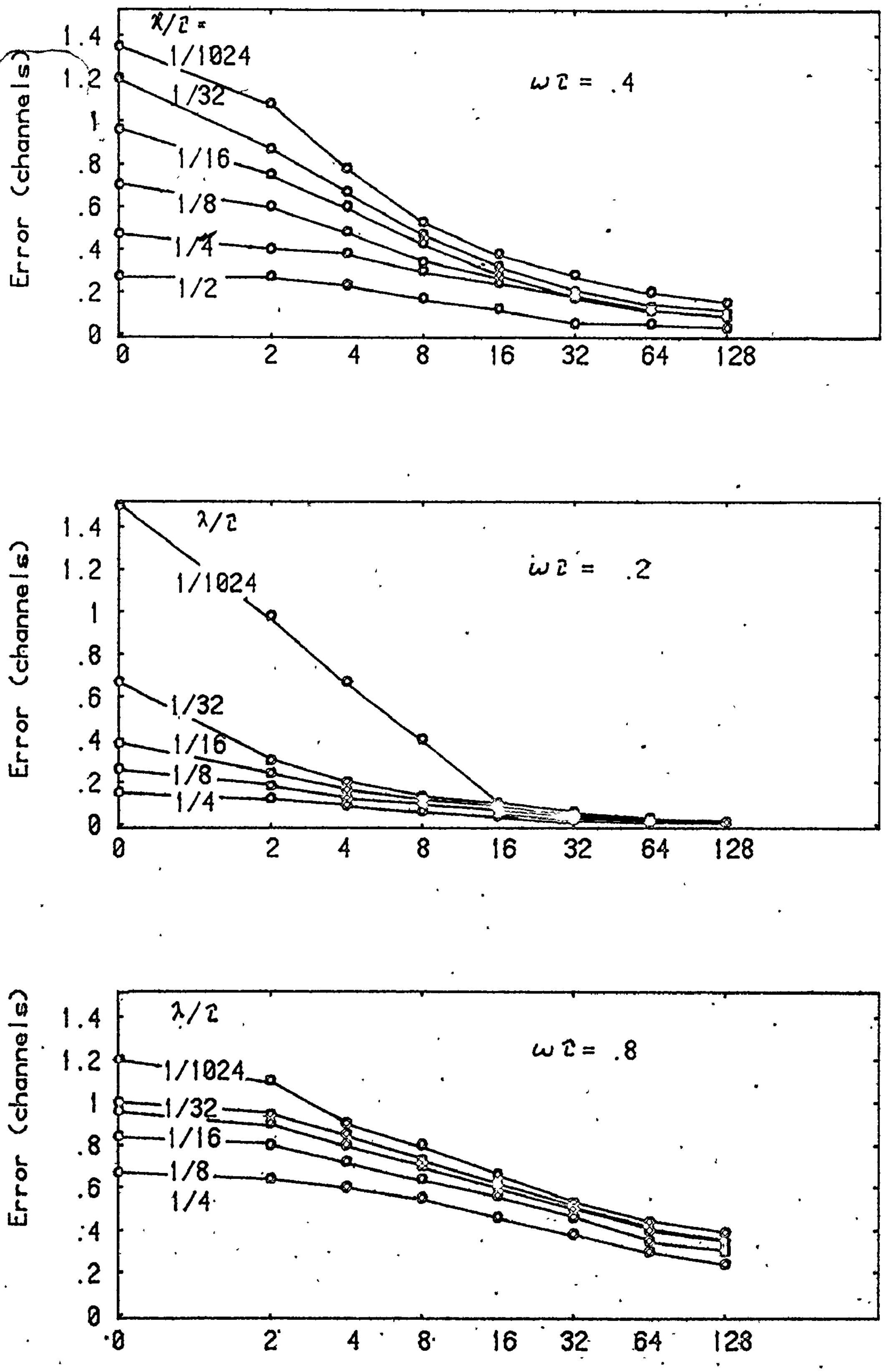

Figure 5-6. Time zero alignment error as a function of the Bayesian iteration index. $\tau = 6$ channels.

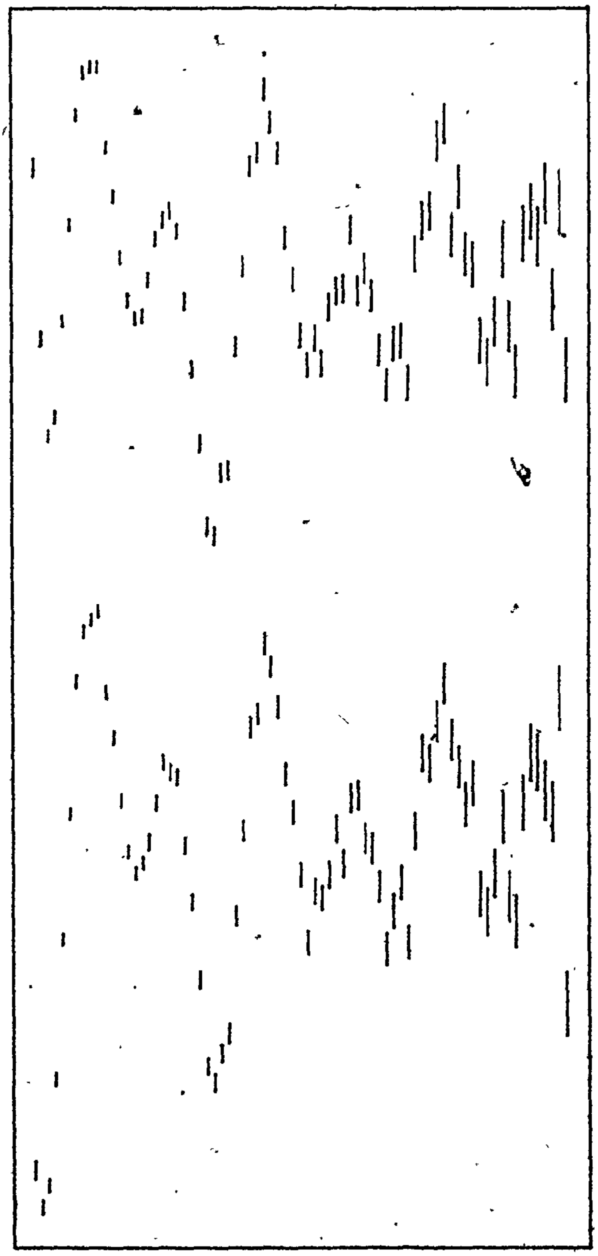

Figure 5-7. The perturbation factor is shown as calculated with and without the extra one channel shift of the 180° time-interval spectrum.

responsible for the undesirable upwards curl of the calculated $G_2(t)$ factors seen in all undeconvolved spectra.

5.4.2 Deconvolution of the Perturbation Factor

The distributive law of the convolution integral allows one to deconvolve either the collected spectra before calculating $G_2(t)$ as examined in the last section or the calculated $G_2(t)$ function directly. Both avenues were explored here, however the latter was preferred because it did not involve a sharp discontinuity near t=0. To be compatible with the collected spectra in which four adjacent channels were summed during the analysis, the time resolution in the following tests was reduced to 6/4 = 1.5 channels. To accommodate the Bayesian approach, the $G_2(t)$ spectra were given a positive bias so that all values were sufficiently positive to allow growth of the negative going excursions.

A typical perturbation factor consists of three frequency components. To be useful, the deconvolution operation must restore the proper amplitudes to each component without introducing any significant amplitude distortion. A test of the Bayesian routine was performed by examining the Fourier power spectra of a series of deconvolved simulated $G_2(t)$ functions. A fully reconstructed signal will contain the same frequency detail as the initial "true" function. Figure 5-8 is an illustration of a

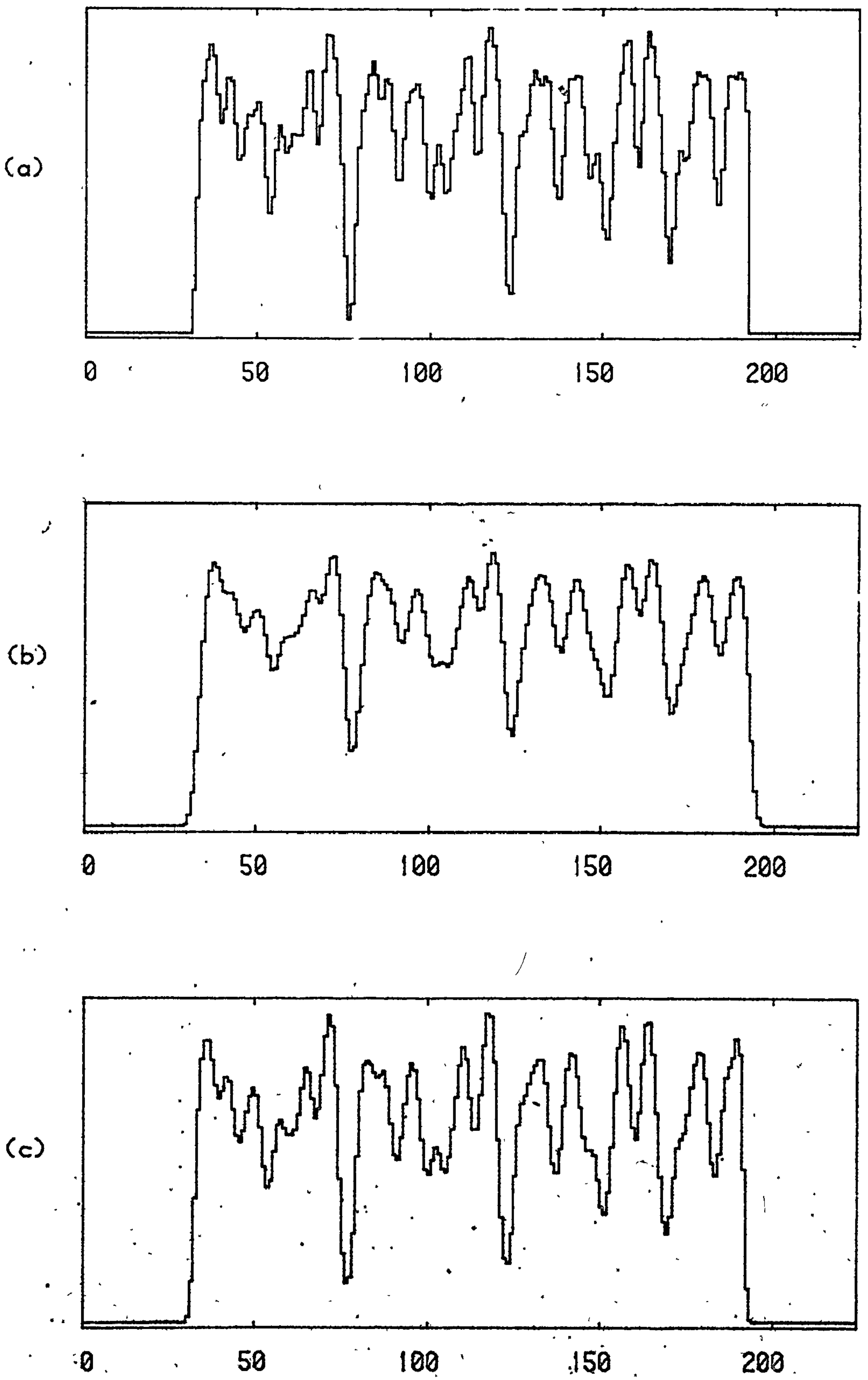

Figure 5-8. The simulated perturbation factor (a) is convolved (b) and then deconvolved (c) with 16 iterations of the Bayesian technique.

simulated perturbation factor during one such test. It was created and convolved with a gaussian curve before being deconvolved with 16 iterations of the Bayesian method. Figure 5-8 (a) shows the initial test function, (b) shows the convolved and (c) the deconvolved forms. Examination of the Fourier spectra show the frequency amplitudes have been fully restored without overshoot. This is best characterized by measuring the frequency response of the process. This can be interpreted as the gain of a convolution and deconvolution operation in succession as a function of signal frequency. Figure 5-9 is a plot of gain vs. frequency resulting from the above series of tests. The linearity of the process at low frequencies and the smooth cut-off at higher frequencies are very noteworthy. This bandwidth improvement can be characterized in terms of the -3dB frequency (the point at which the amplitude drops to $1/\sqrt{2}$ of the zero frequency value) and is directly related to the factor of improvement in the effective time resolution shown in figure 5-10.

If the spectra contained little or no statistical noise, each could be deconvolved until the desired improvement was obtained. In practice, high frequency noise grows more quickly than signal reconstruction and some optimum number of iterations must be chosen. If the final true form of the perturbation factor were known a priori, the cut-off

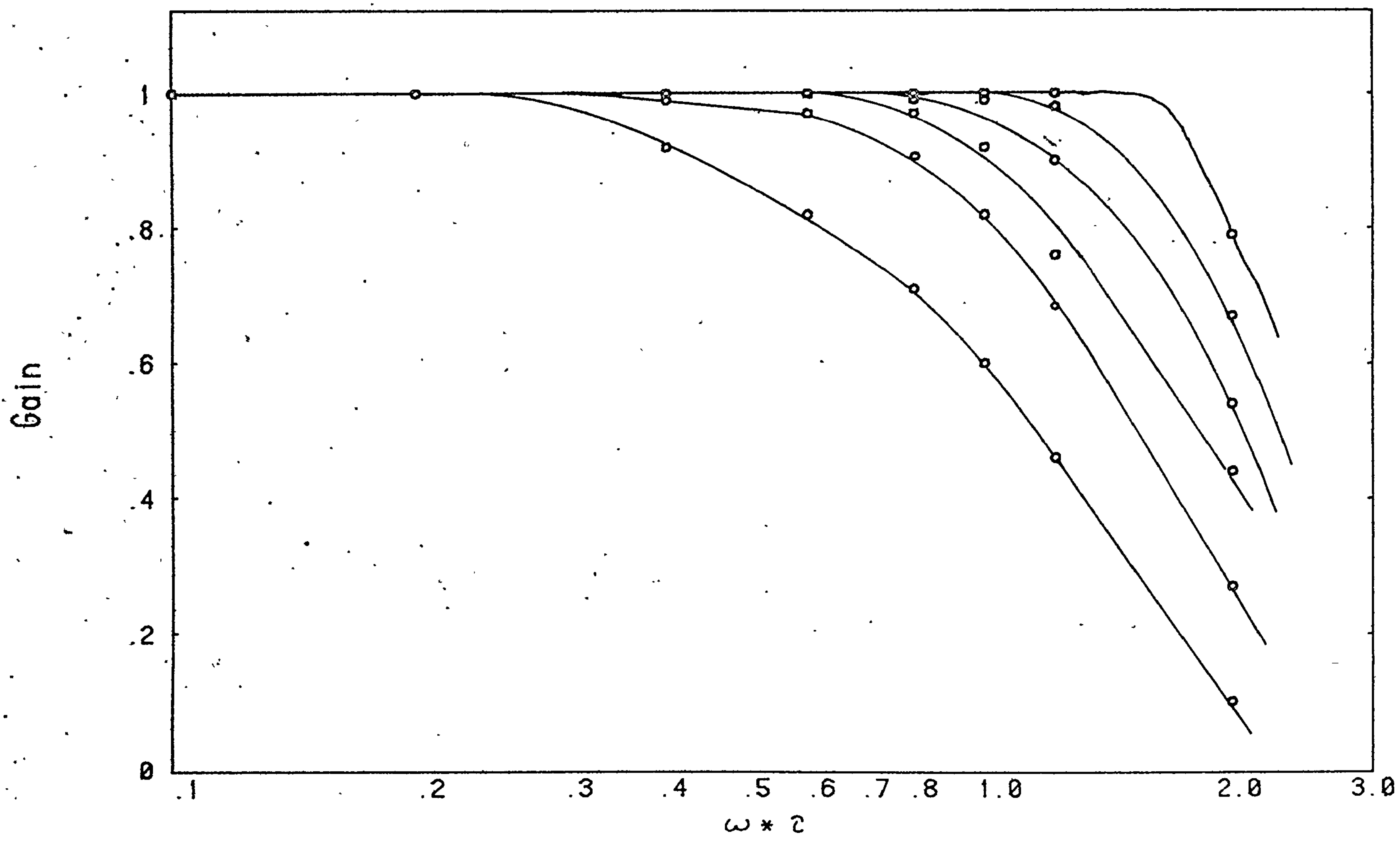

Figure 5-9. Frequency response of the convolution / deconvolution process as a function of the frequency-time resolution product.

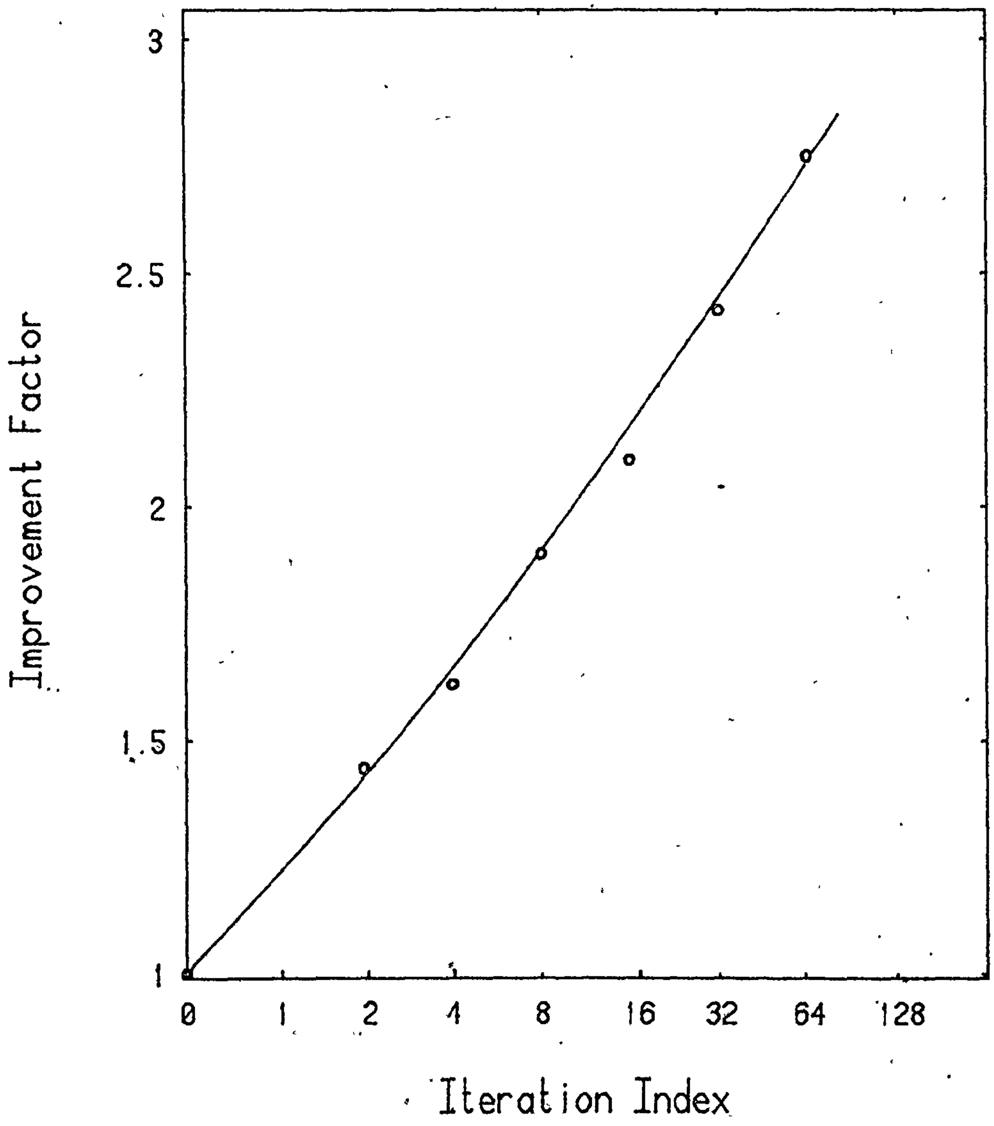

Figure 5-10. Factor of improvement in the effective time resolution from the Bayesian deconvolution process.

point could be chosen by minimizing the weighted expectation value of the variance between the true and deconvolved spectra. Thus after ν iterations

$$X^2 = \left\langle \frac{(I-D^\nu)^2}{I} \right\rangle \qquad (5\text{-}12)$$

is a minimum where I and D^ν are the ideal and deconvolved spectra respectively. In practice only the observed data with noise and the response function are known. As suggested by Kennett and Prestwich (Ke79), a test that can be performed is to convolve the response function into the partially deconvolved spectra and compute the value of

$$X_0^2 = \left\langle \frac{(M-R*D^\nu)^2}{M} \right\rangle \qquad (5\text{-}13)$$

where M is the observed data and R the response function. X_0^2 shows an initial decrease with ν while signal improvement predominates and levels out when noise growth becomes excessive. Figure 5-11 shows X^2 and X_0^2 curves for the test data used in figure 5-9. X_0^2 decreases quickly with ν until X^2 reaches a minimum. At this point X_0^2 is approximately unity and any further reduction is due to noise movement and not signal improvement. An estimate of noise growth was made by creating a spectrum with Poisson noise only and calculating the value of

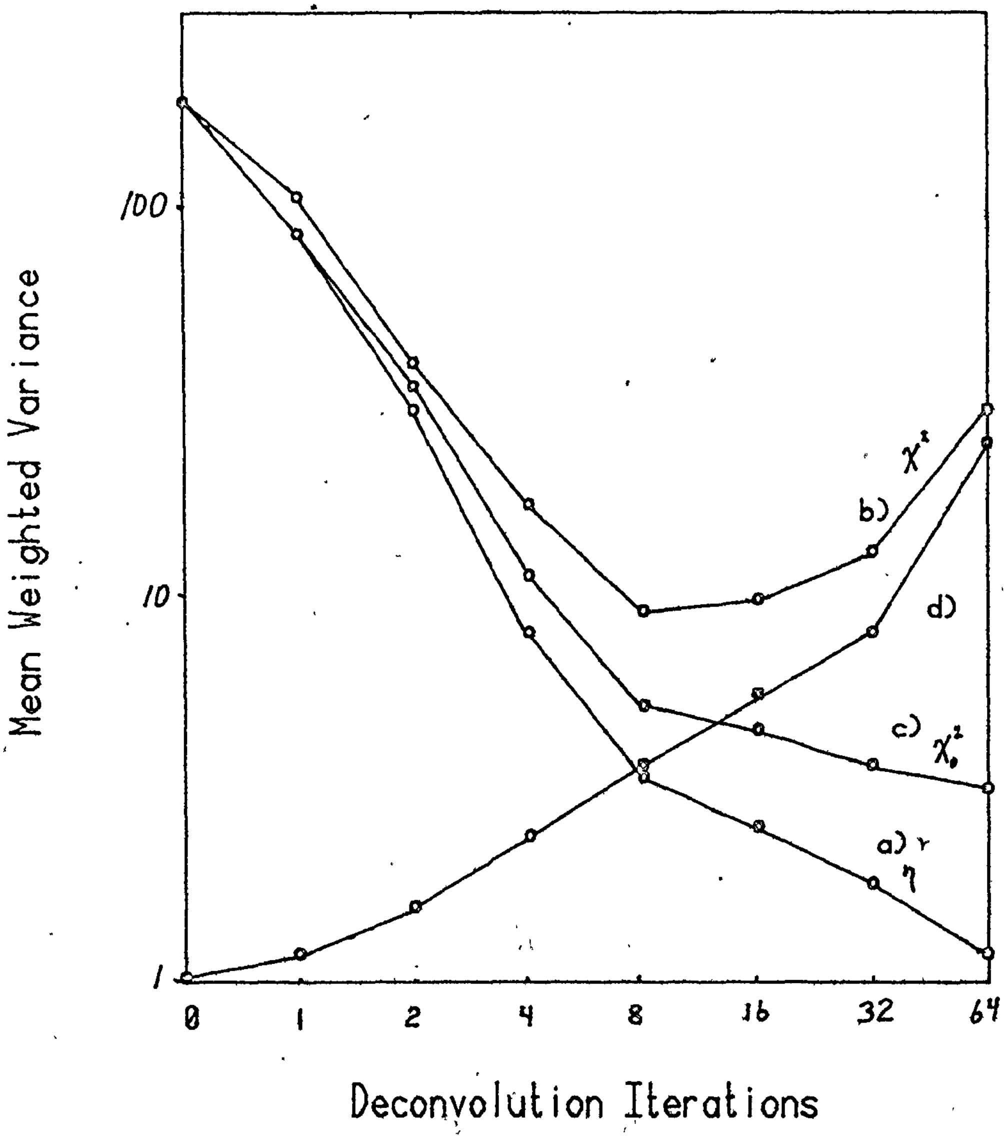

Figure 5-11. Noise properties of deconvolved spectra. The four curves are defined in the text as the expectation value of the variance a) between the true and deconvolved spectra η, b) between the true and deconvolved with noise χ^2, c) between the observed and convolved/partially deconvolved χ_0^2 spectra and d) of noise growth.

$$N = \left\langle \left\{ \frac{D^{\nu} - \sigma}{\sigma} \right\}^{2} \right\rangle \qquad (5\text{-}14)$$

where σ is the mean (and standard deviation) counts per channel. Neglecting the background component, σ varies as

$$\sigma(t) = \frac{1}{3\sqrt{N_0}} e^{\lambda t/2} \qquad (5\text{-}15)$$

where N_0 is the maximum number of counts per channel near t=0, typically 150,000. As shown in figure 5-11, N is initially one and grows quickly with ν. When X_0^2 approaches unity, noise growth is masking signal improvement and the deconvolution process should be halted (found to be approximately 16 iterations in the presented data). For reference, figure 5-11 includes a line labeled η defined as

$$\eta = \left\langle \frac{(I-D^{\nu})^2}{I} \right\rangle \qquad (5\text{-}16)$$

where again I is the idealized spectrum and now D^{ν} is the deconvolved noise free spectrum. This is a measure of signal reconstruction.

It is clear from the above tests that this deconvolution approach is a potentially very interesting tool. A deconvolver's greatest foe however is spectral noise and all practical steps should be taken in designing the experiment to give the best possible counting statistics.

CHAPTER 6

EXPERIMENT RESULTS

6.1 Calculation of the Perturbation Factor

Spectra such as the two shown in figure 6-1 were collected in daily runs at both emission angles and recorded individually. The SCA scaler total count was recorded for each detector and used to normalize the two spectra, a correction which was usually less than 2%. All spectra at each of the fifteen sample temperatures examined were shifted in time by an integer number of channels to align the half maximum points and spectra collected at the same emission angle were summed. After subtracting the background accidental coincidences using the method of equation (4-9), the 180° spectra were given an additional one channel shift (section 5.4.1). All spectra were compressed by a factor of four on the time axis to give the best possible counting statistics and the attenuated perturbation factors (section 4.2) were calculated as

$$A_2' G_2'(t) = \frac{2(W(180,t) - W(90,t))}{W(180,t) + 2W(90,t)}. \qquad (6\text{-}1)$$

6.2 Results of the Fourier Analysis

The Fourier transform analysis was performed on the

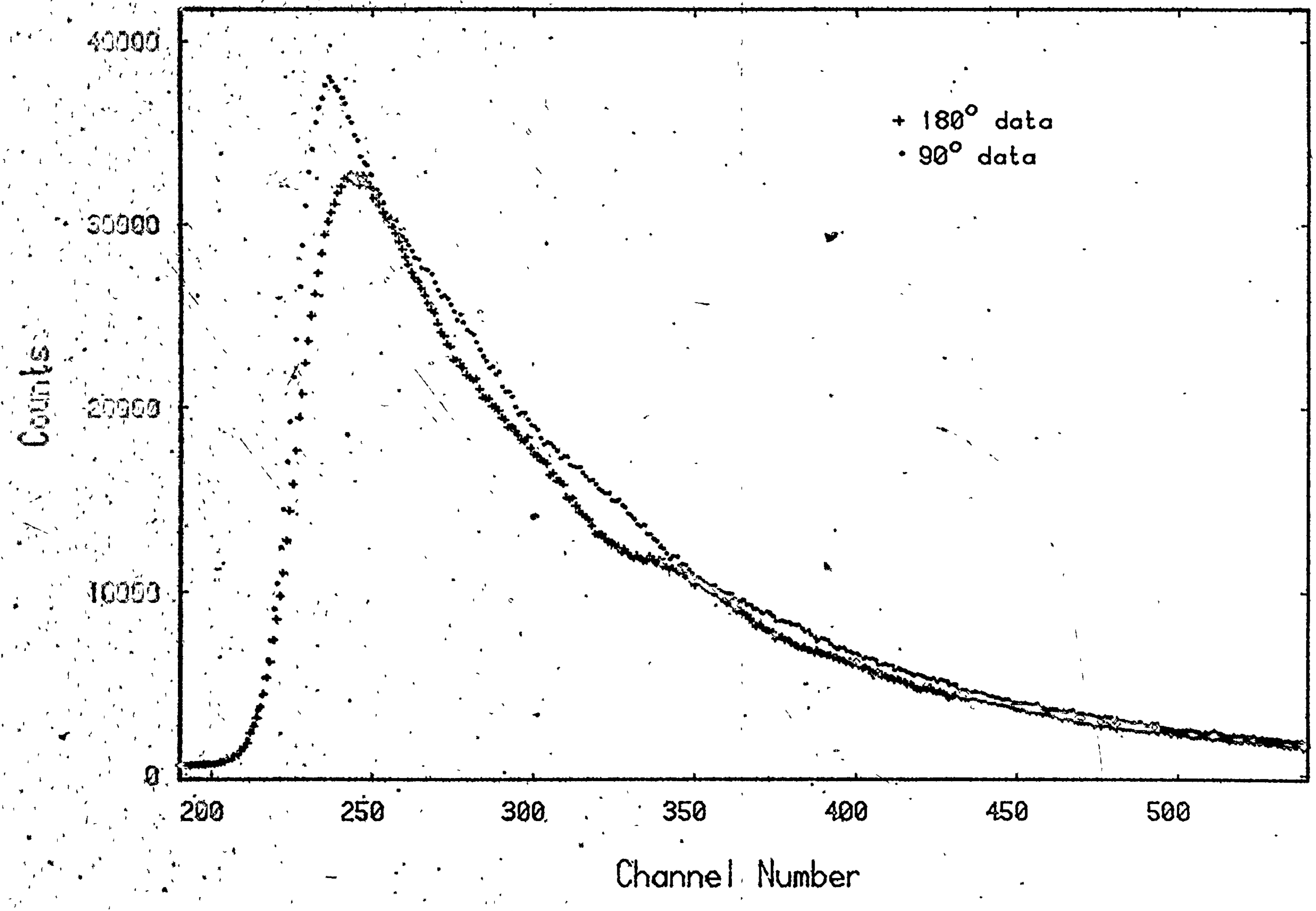

Figure 6-1. Sample time interval-spectra. Background coincidences were estimated in regions well before and well after the exponential.

perturbation factors to identify the frequency components present. This provided an estimate of the frequencies ω_1, ω_2 and ω_3 independent of all other parameters. Because of a large degree of overlap it was not always possible to separate the higher frequency components. However the fundamental frequency, ω_1, could always be identified and was used as the first estimate in the least squares fitting procedure.

The transform analysis was probably more important in identifying the number of frequency components. Figure 6-2 shows a series of the perturbation factor transforms over the temperature range 138 to 318 K. The low temperature spectra show more than three frequency components suggesting there is more than one possible site for the hafnium nucleus in this compound.

One of the components, identified as the ω_2 term of the second site in the least squares analysis, is seen to shift towards decreasing frequency with increasing temperature until it overlaps with the fundamental frequency component at approximately 230 K. Since the relationship of ω_2 to ω_1 is determined by the asymmetry parameter alone (figure 2-4), this result indicates that the asymmetry term increases with temperature in this range to a value of about one. The same result is seen in the time domain analysis.

Evidence for another structural change is strongly

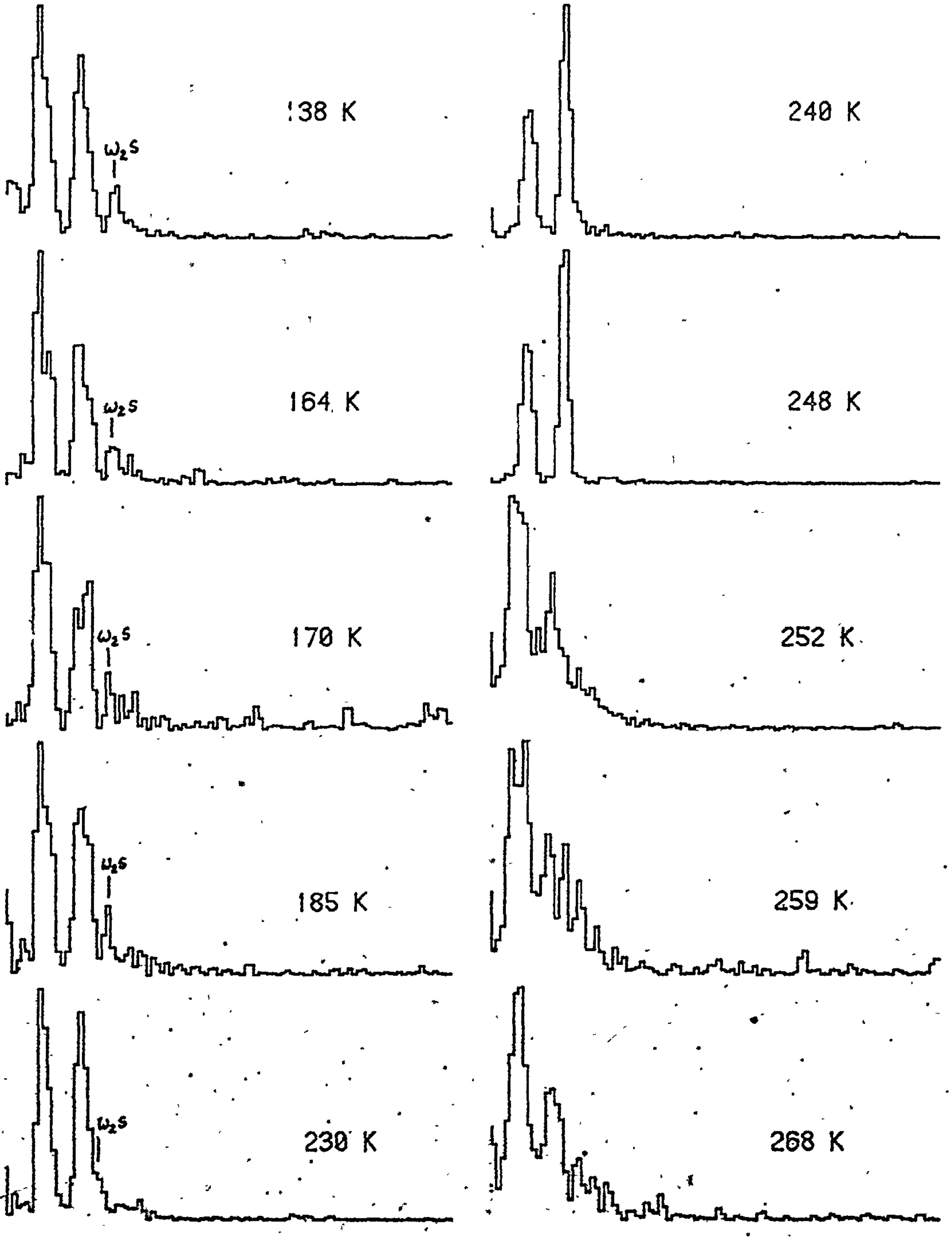

Figure 6-2. Frequency power spectra of the perturbation factors using the weighted least squares technique.

suggested between 248 and 252 K. The frequency spectrum changes drastically from a few well defined components to three (although not obviously) on a large background continuum. This spread in frequencies is caused by the exponential relaxation due to a dynamic electric quadrupole interaction (section 2.3.2), an effect better seen in the time domain analysis. The shape of this frequency distribution is given by the convolution integral of the transform of the static interation with that of an exponential function, a Lorentzian distribution;

$$\mathcal{F}\left\{G_2^{static}(t)\right\} \;*\; \left\{\frac{1-\frac{2\pi is}{\lambda}}{1+\left\{\frac{2\pi s}{\lambda}\right\}^2}\right\} \qquad (6\text{-}2)$$

where λ is the relaxation constant.

It should be mentioned that the least squares Fourier transform has been used here. The high noise content in the measured data produced anomolous components and masked others in the traditional transform.

6.3. Results of the Deconvolution Analysis

The deconvolution techniques described in the last chapter were applied in an analysis of the fifteen composite perturbation factors. Figure 6-3 shows one of the $G_2(t)$ functions before and after 16 iterations of the Baysian deconvolution operation. In this example the effective time

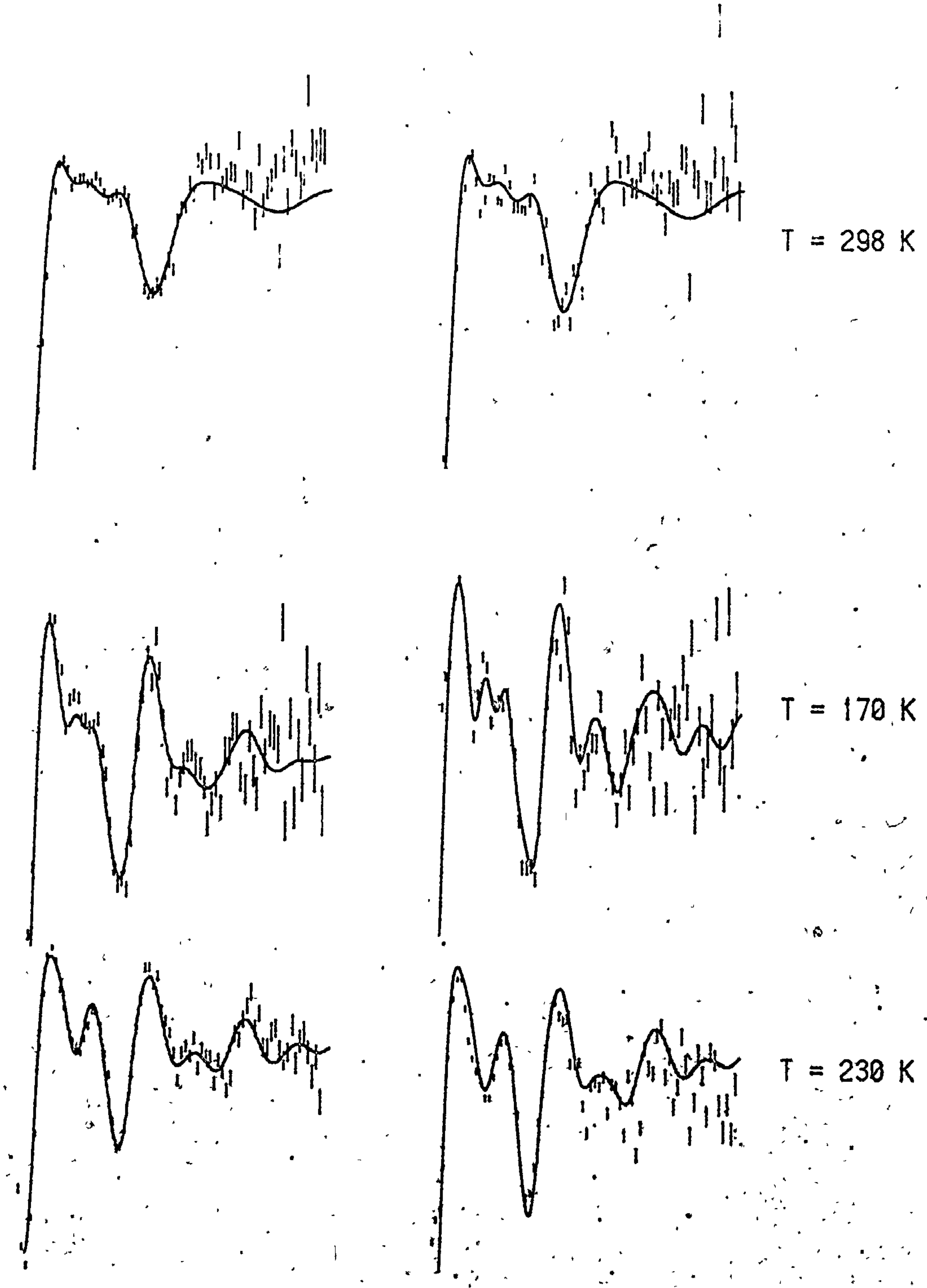

The measured perturbation factors.

The measured perturbation factors after 16 iterations of the Bayesian deconvolution process.

Figure 6-3: Deconvolution of measured perturbation factors. The vertical bars represent plus and minus one standard deviation from the measured value. The solid line resolution of the measurement has been reduced from 2.1 ns to 1.0 ns (estimated using figure 5-10). The solid lines in figure 6-3 represent the least squares fitted curves. In the least squares analysis of the deconvolved data, no correction for finite time resolution was made to the model. The restored high frequency components can be seen most clearly near t=10 ns, illustrating excellent agreement between the deconvolved data and the uncorrected model. Both approaches yielded parameter values consistent with each other within statistical uncertainties in all fits. This consistency builds confidence that the parameters have been properly evaluated in the fitting procedure and the effect of a finite time resolution has not been confused with, for example, a finite frequency distribution. Such a verification is the only real benefit from a deconvolution analysis. There is no significant improvement in parameter uncertainties because the decrease resulting from one less degree of freedom is offset by the increase due to a larger spectral noise content. This result must be expected since the deconvolution process does not add new information; it only redistributes it.

The importance of deconvolving would be greater if the ω_2 term was at a high enough frequency to be severely attenuated (ie. $\omega_2 \geq 1.5$ Grad/s). This would leave only the fundamental component identifiable and insufficient information to calculate all frequencies. (The ω_3 term can normally be found with the triangulation constraint on the frequencies even if it has been filtered.) In this study the highest ω_2 component observed is 1.0 Grad/s and the highest ω_3 term is 1.8 Grad/s.

6.4 Results of the Least Squares Fitting Analysis

Estimates of the values of the parameters describing the electric quadrupole interaction, namely ω_1, η, δ, A_2, a d.c. term, a small time shift and the relaxation constant, λ_k, were made using a rapidly converging non-linear least squares fitting routine (Da59, F163). This process involved minimizing the reduced chi squared error between the measured data and the theoretical expression which is defined as

$$\chi^2 = \frac{1}{N-\nu} \sum_i \frac{(G_2(i) - y_i)^2}{\sigma_i^2} \qquad (6\text{-}3)$$

where N is the number of data points (y_i) with variance σ_i^2 and ν is the number of parameters being fitted. In general this type of analysis runs the risk of being somewhat subjective because it is strongly influenced by the form of the model used; it is always possible to get an arbitrarily good fit by introducing a sufficient number of parameters. In the following analysis the minimum number of terms possible from a physical point of view that will properly describe the features observed (at least qualitatively) were used.

The starting value of each parameter can influence the final results if a solution is not unique. Here the initial ω_1 value was obtained from the Fourier study, η was started at random values between zero and one and always converged to a unique result and δ was started as zero and remained small in all spectra. The time resolution was measured directly (chapter 4.1) rather than fitted as a free parameter.

Figures 6-4a and 6-4b show some measured perturbation factors and the least squares fitted functions. These evaluated parameters are shown in figures 6-5 to 6-9. The two structural re-arrangements in the K_3HfF_7 sample suggested in the Fourier analysis section are evident. Above a critical temperature of 250 ± 1 K a one site model which included a relaxation term was sufficient to make a good fit while below this point a two site model was required and the relaxation term was not. The relative population of the higher probability site below 250 K was fitted as a free parameter and remained constant at 0.74 ± .02 suggesting a 3:1 occupation ratio. Above the critical temperature it was fixed as one to evaluate ω_1, η and δ and did not change significantly even when allowed to vary.

The fundamental frequency of both sites remained constant below 250 K, however the EFG asymmetry of the lower

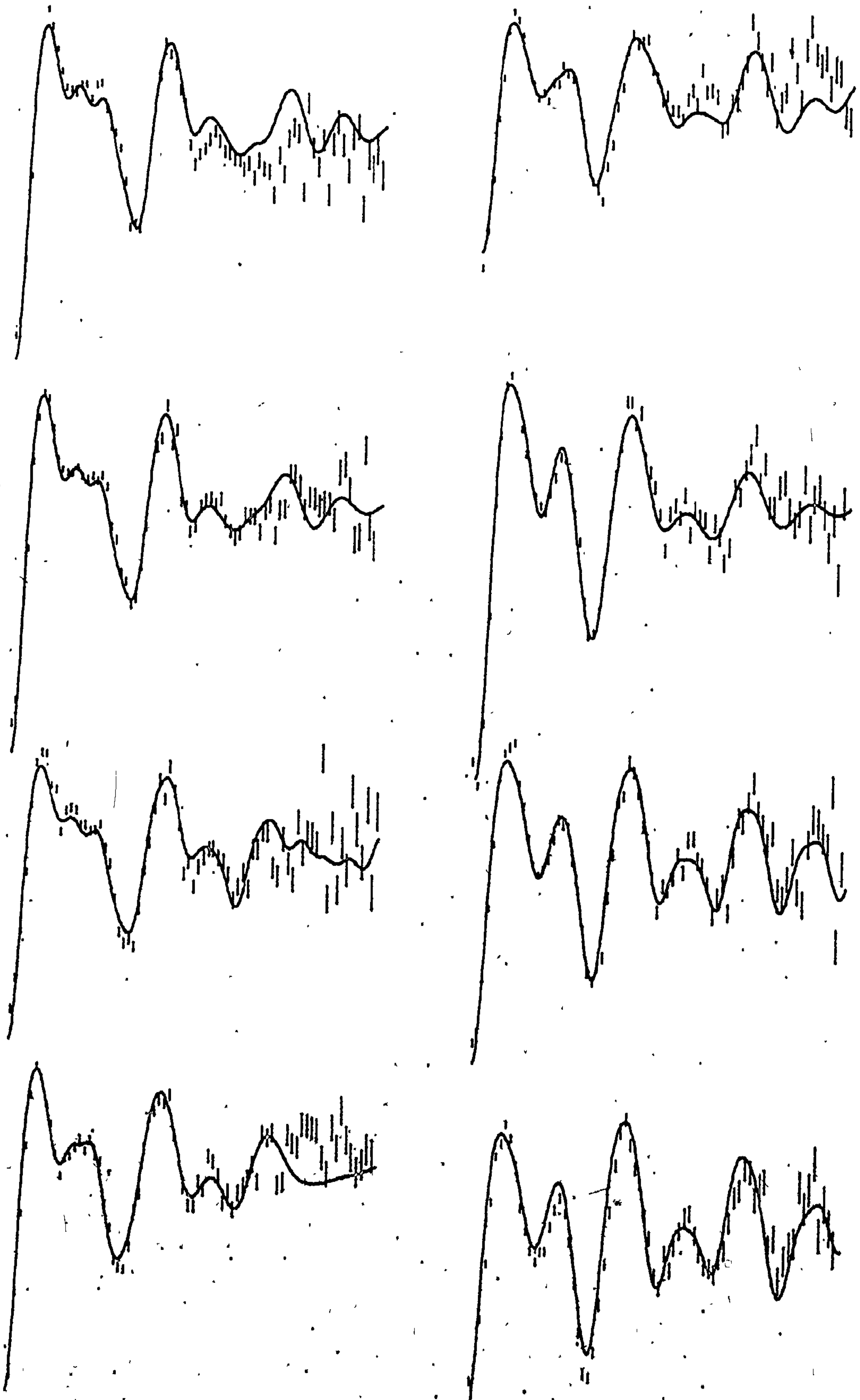

Figure 6-4a. Measured perturbation factors from 138 to 245 K. The vertical bars represent plus and minus one standard deviation, the solid line is the fitted function.

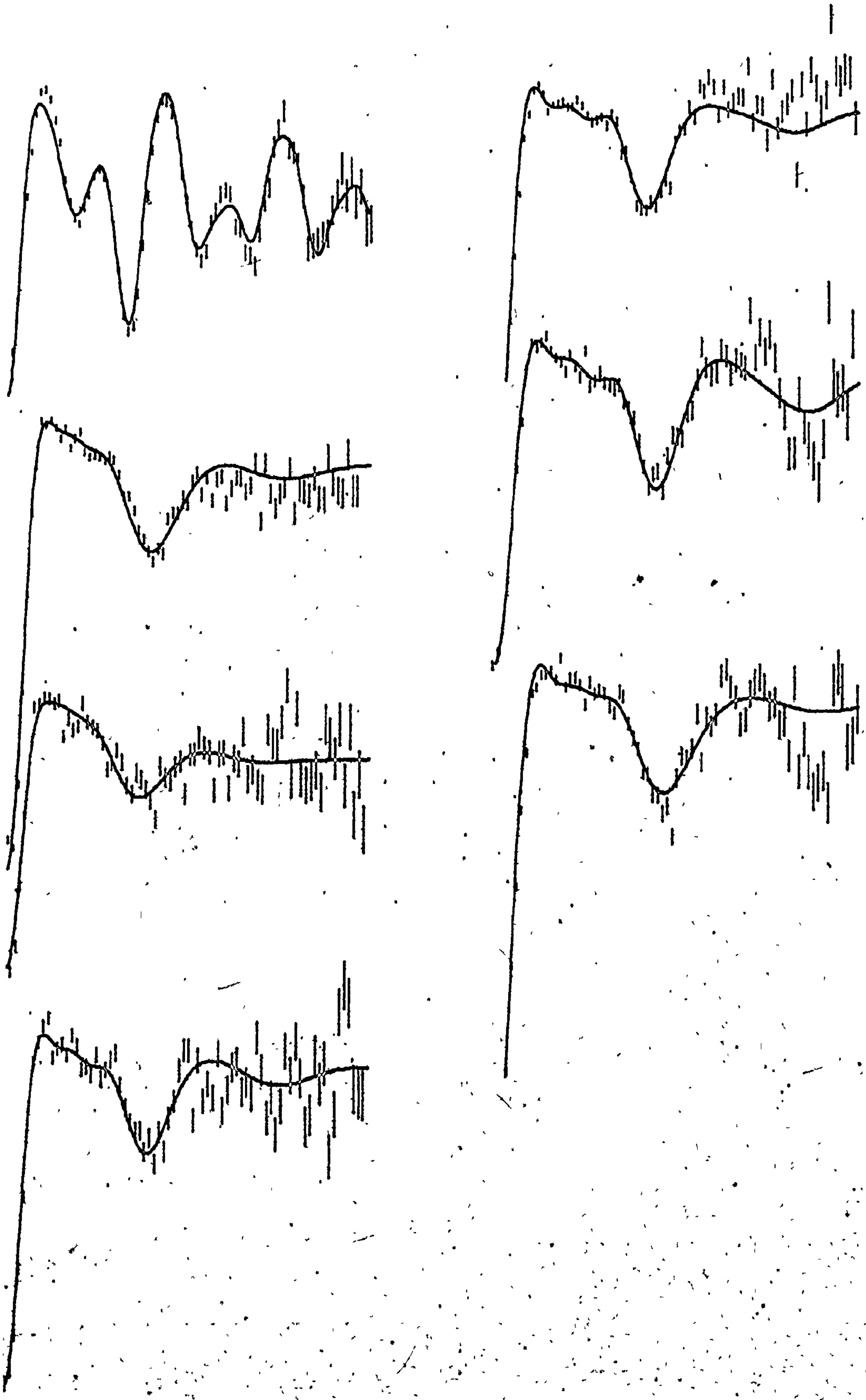

Figure 6-4b. Measured perturbation factors from 248 to 310 K.

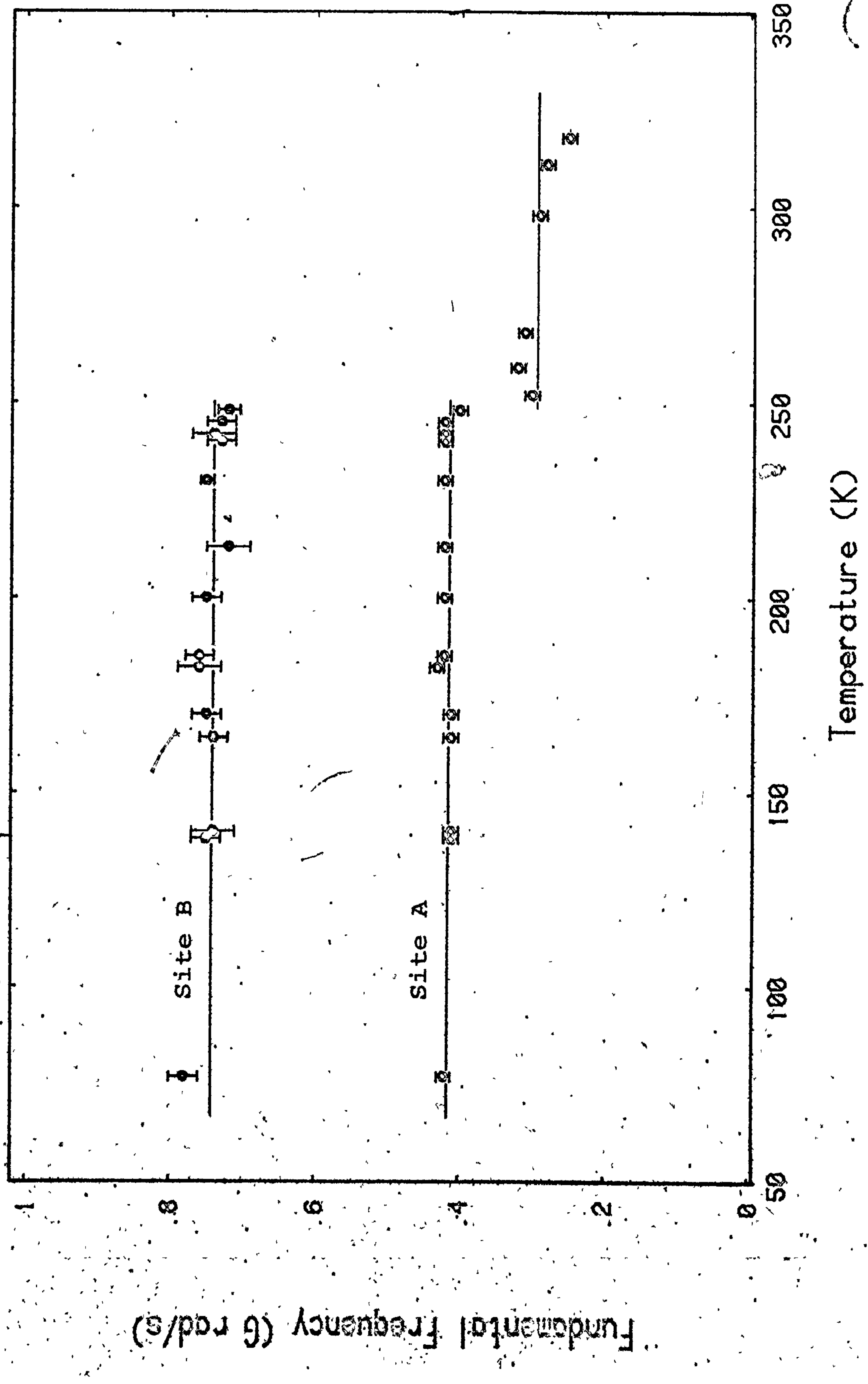

Figure 6-5. The fitted fundamental frequency w_1.

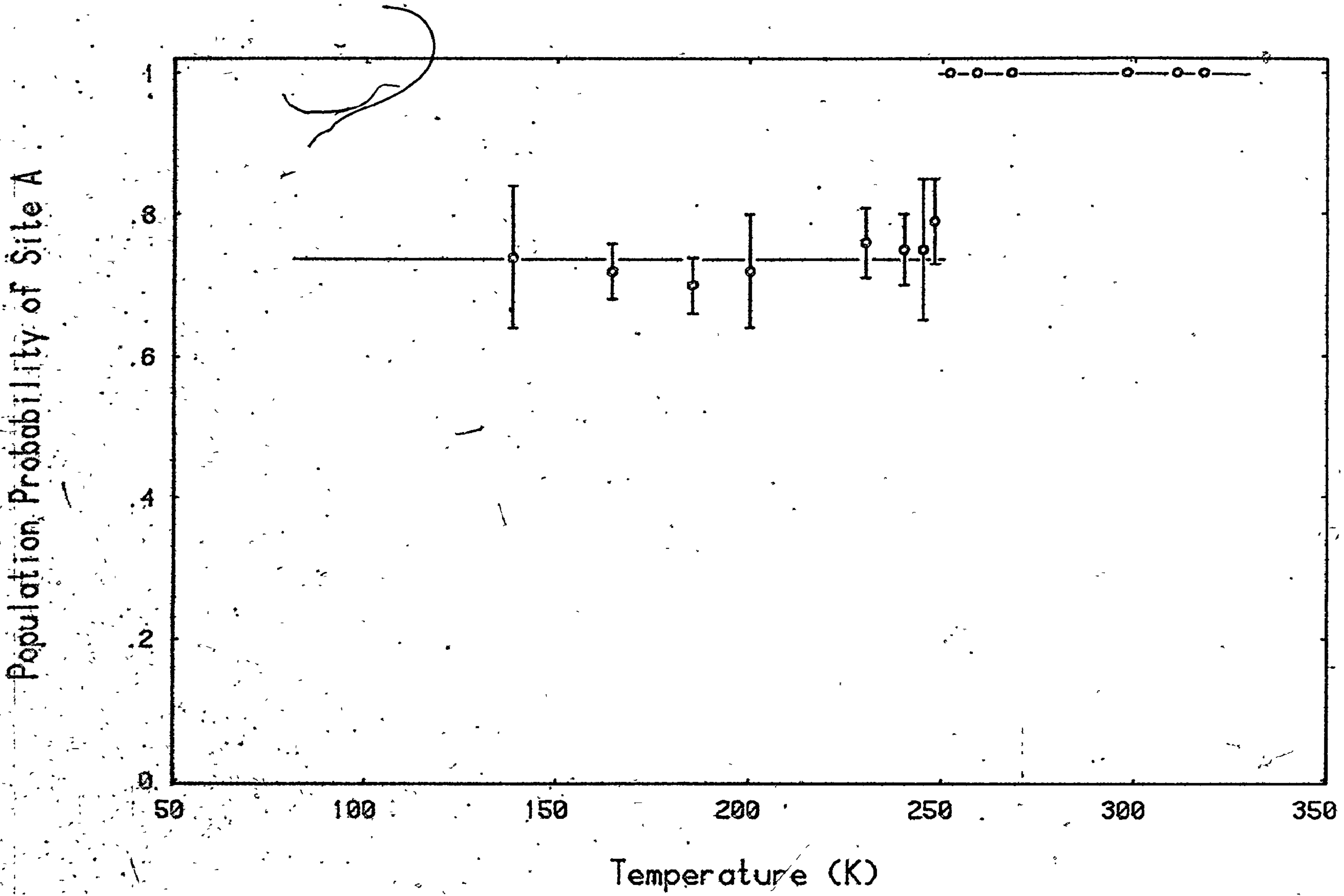

Figure 6-6. The population probability of site A. Only those values showing error bars were evaluated as a free parameter.

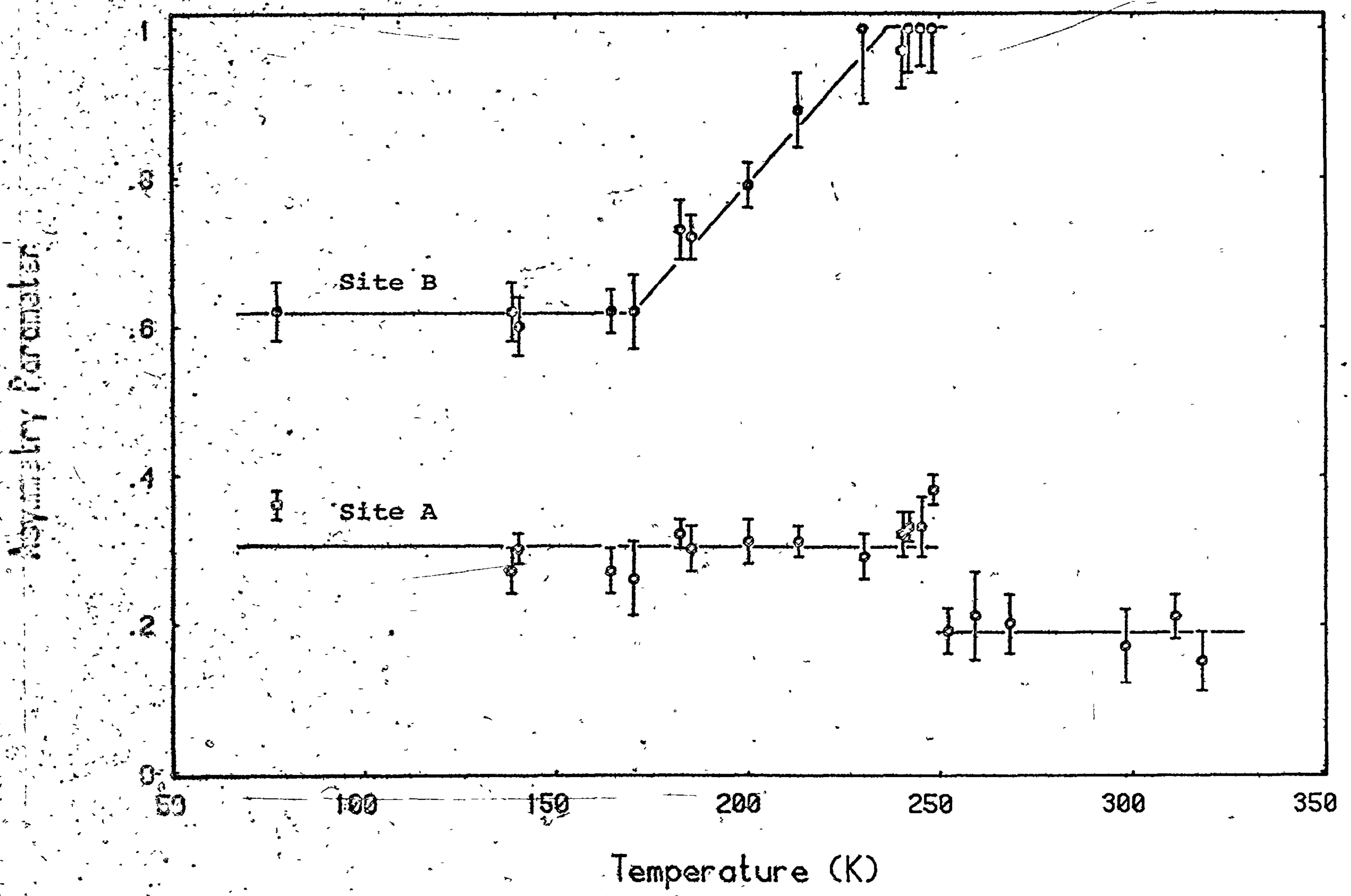

Figure 6-7. The fitted asymmetry parameter.

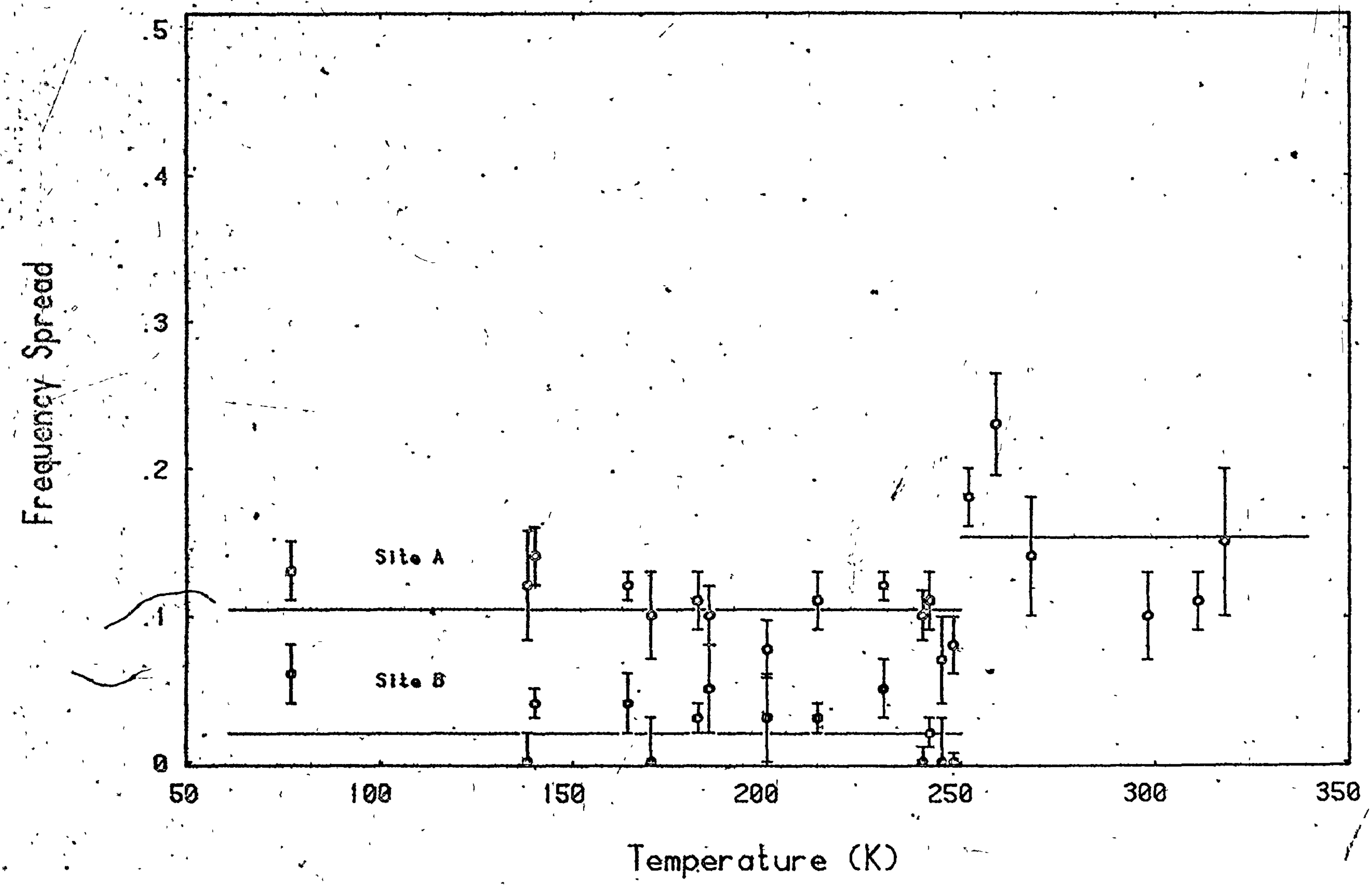

Figure 6-8. The fitted frequency spread.

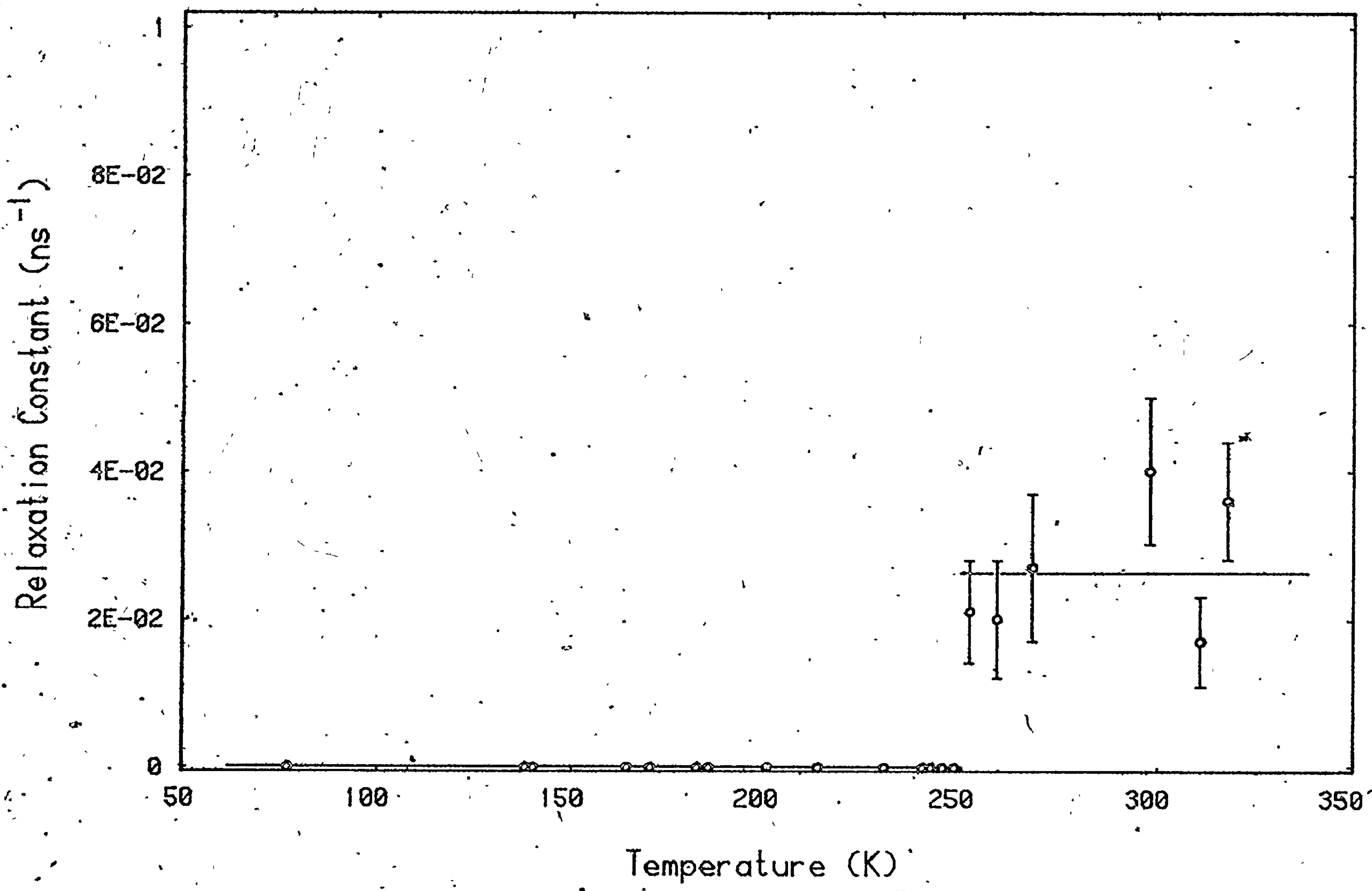

Figure 6-9. The relaxation constant. Only those values showing error bars were evaluated as a free parameter.

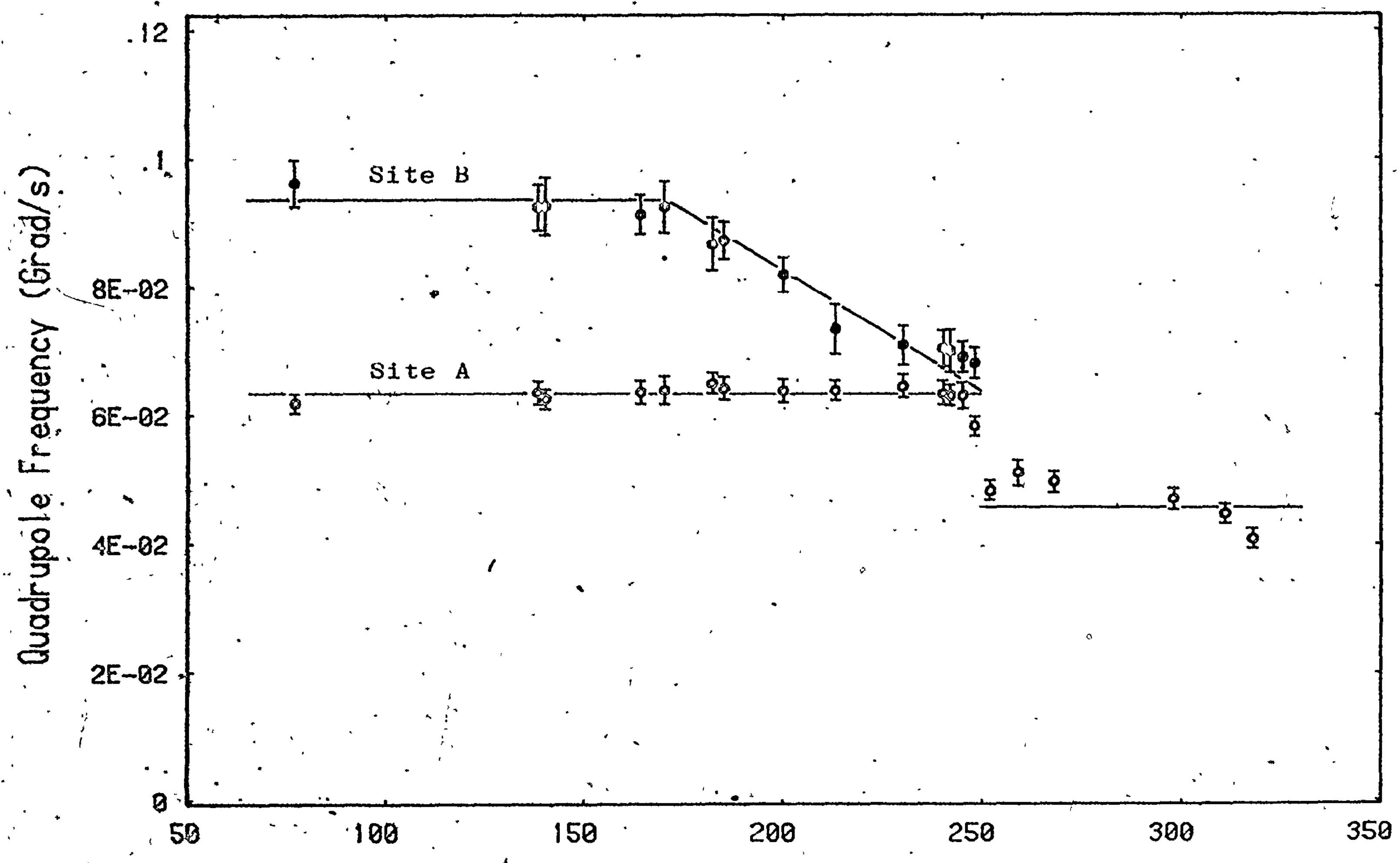

Figure 6-10. The calculated quadrupole frequency w_Q

probability site B increased from 0.62 ± .02 to $\eta > 0.98$ between the temperatures 170 and 230 K respectively. In all cases η remained less than or equal to one without requiring a constraint condition in the fitting program.

The frequency spread parameter of site B did not show the temperature dependence exhibited by the asymmetry but remained constant below 250 K with an average of 0.007 ± 0.001. The site A asymmetry was temperature independent at 0.08 ± .01 below the critical temperature and the one site spread above it was 0.15 ± .01.

The relaxation term in the high temperature phase appeared to show a slight increase with increasing temperature, although the large uncertainties preclude any definitive conclusion. A summary of the evaluated parameters is presented in table 6-1.

6.5 Discussion

A transition from a two site to a one site environment for the hafnium atom in K_3HfF_7 as the temperature increases is compatible with the results of x-ray studies on the similar compound K_3ZrF_7 by Buslaev et al. (Bu71). They reported a transition from an orthorhombic modification at 77 K to a cubic lattice at room temperature. Boyer et al. (Bo76) performed a TDPAC study on Na_3HfF_7 and saw a two to one site transition between 375 and 455 K. They suggest

Sample	Temp (K)	ω_1 (Grad/s)	η	ω_Q (Grad/s)	$/V_{zz}/$ ($\times 10^{17} V/cm^2$)	popul.	ref.
K_3HfF_7	138–248 (site A)	.414±.006	.32±.04	.062±.002	6.5±.2	.74±.02	present study
"	138–170 (site B)	.74±.01	.62±.03	.091±.003	9.6±.4	.26±.02	"
"	230–248 (site B)	.74±.01	>.95	.071±.002	7.5±.4	.26±.02	"
"	252–318	.29±.02	.19±.03	.047±.004	4.9±.8	1	"
K_3HfF_7	77 (site A)	.416±.008	.36±.02	.061±.002	6.4±.4	.66±.04	Lo77
"	77 (site B)	.78±.2	.62±.04	.096±.005	10.1±.7	.34±.04	"
"	294	.281±.007	.17±.02	.045±.001	4.8±.3	1	"
Na_3HfF_7	296 (site A)	.660±.008	.40±.05	.095±.004	10.0±.4	.50±.03	Bo76
"	296 (site B)	.860±.009	.15±.07	.140±.004	14.7±.4	.50±.03	"
"	453	.353±.003	.19±.03	.057±.001	6.0±.2	.78±.02	"
K_3HfF_7 (Mossbauer)	4				6.4±.3	1	Ge71

Table 6-1. Comparison of experiment results with previous studies.

this is the result of an orthorhombic-tetragonal transition in the crystal structure.

The mechanisms of such a transition cannot be determined unambiguously from a TDPAC study; a careful x-ray analysis with changing temperature is required. It is useful however to interpret the present results in light of some proposed structures. The hafnium atom is known to exist in the complex radical HfF_7^{3-} (An70) which in turn fits into the crystal structure. There are three known forms for such a coordination seven radical (Co66):

a) a disordered pentagonal bipyramid,

b) a trigonal prism distorted to accomodate the seventh fluorine atom on one of the three rectangular faces, and

c) an octahedron in which the seventh fluorine atom is located in the center of one face.

The octahedron model can be ruled out on two grounds; a) ~~Hurst~~ and Taylor (Hu70) showed results from an x-ray analysis of $(NH_4)_3ZrF_7$ that were incompatible with such a model and b) the octahedron has cubic symmetry which would not produce an electric field gradient at the hafnium site. Hurst and Taylor found also that the trigonal prism model could not be fitted to their observations. They suggest the most likely configuration is a disordered pentagonal bipyramid in which two of the fluorine-zirconium distances are greater than the other five and the five points of the pentagon are distorted from their plane. This form would support a static interaction because it is stable and has no cubic symmetry.

A model of this ion, shown in figure 6-11, was made of a distribution of point charges. The values of η and V_{zz} were calculated (appendix II) to be 2×10^{16} V/cm^2 and 0.82 respectively and can be compared with measured values in table 6-1. Such a crude model gives only an order of magnitude estimate of V_{zz} but gives some insight into the behaviour of η. The distortion of the pentagonal bipyramid results from fitting the ion into the lattice site. As such, it is possible there is a distribution of fluorine coordinates. The effect of this distribution on η and V_{zz} was estimated in a Monte Carlo simulation by varying the angular coordinates of those fluorines distorted from a regular pentagon by an amount $\Delta\Omega$. The corresponding distributions in the three field gradients and interaction frequencies are shown in figure 6-12 for $\Delta\Omega = 1^\circ$. It was found that:

a) η is moderately sensitive to $\Delta\Omega$ ranging from 0.8 ± 0.1 to 0.7 ± 0.2 for spreads of $\pm .5^\circ$ and $\pm 2^\circ$ respectively.

b) The fundamental frequency was independent of $\Delta\Omega$ within statistical uncertainties.

c) The frequency spread was approximately gaussian shaped for both a gaussian and rectangular distribution in

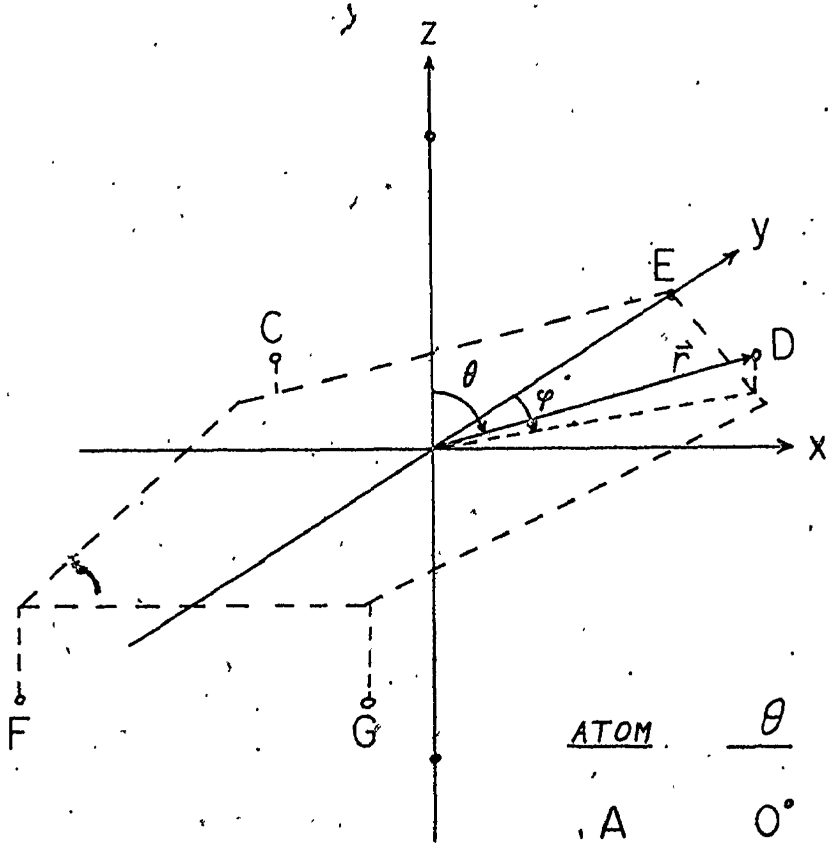

ATOM	θ	φ	$\lvert\vec{r}\rvert$
A	0°	0°	2.00 Å
B	180	0	2.00
C	88.1	-79.8	2.00
D	88.1	79.8	2.00
E	90	0	2.00
F	98.4	-135.6	2.07
G	98.4	135.6	2.07

Figure 6-11. The distorted pentagonal bipyramidal structure of HfF_7^{3-}. The hafnium atom is at the origin.

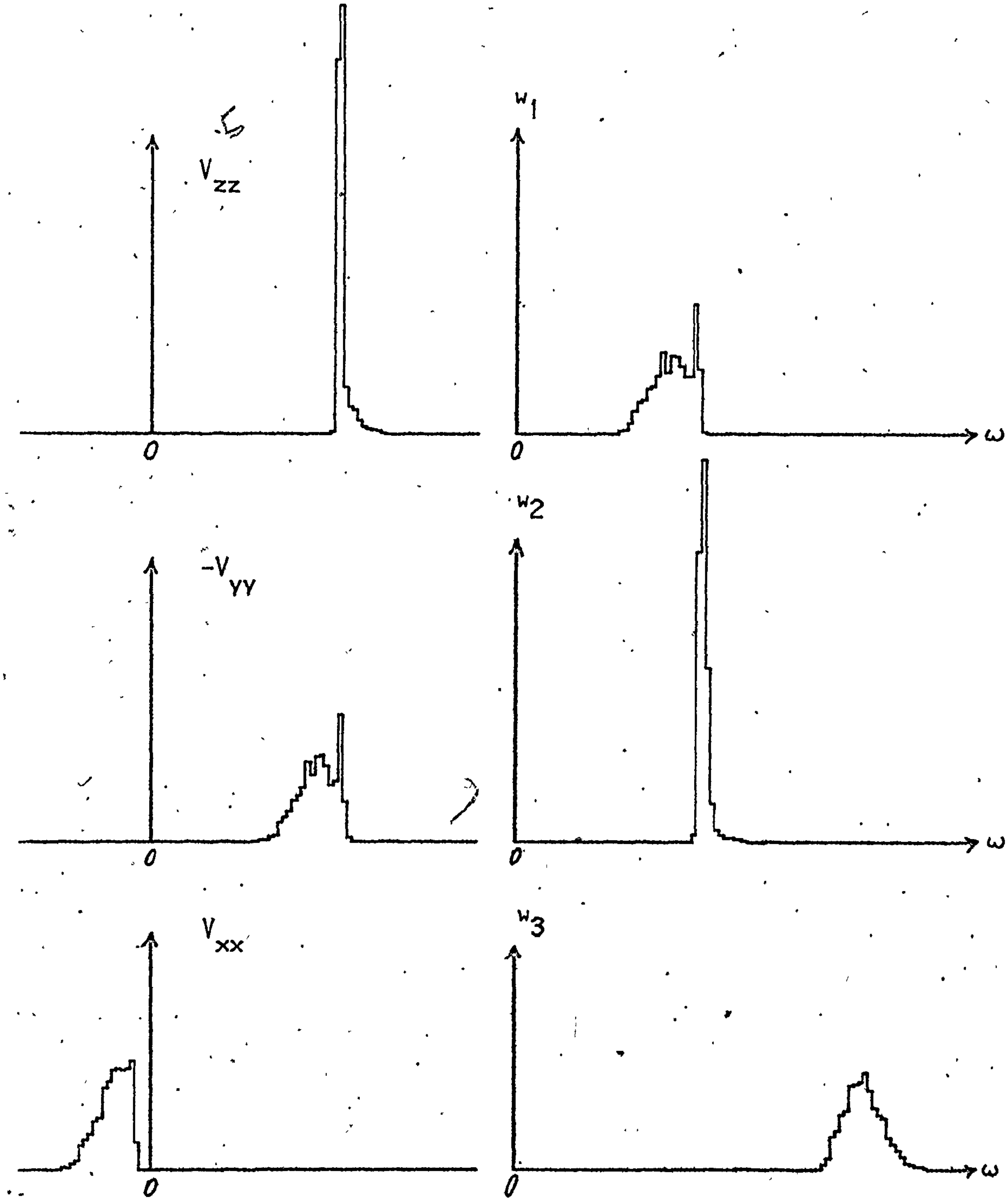

Figure 6-12. Distributions in the EFG and interaction frequencies for the distorted bipyramidal model with $\Delta\Omega = 1°$.

$\Delta\Omega$ for $\Delta\Omega < .5^o$. The three components did not have the same widths for any case.

Point a) is a consequence of defining the asymmetry between 0 and 1; the wider a distribution becomes, the further the average will be from its extremes. Forker (Fo73) has suggested using a model in which the EFG components V_{zz}, V_{yy} and V_{xx} have a gaussian distribution with widths Δ_{zz}, Δ_{yy} and Δ_{xx} rather than the conventional approach used in this study of assuming the same gaussian distribution in all frequencies. He calculated the corresponding $G_2(t)$ factors and made a least squares fit of the parameters ω_1, η and δ. The difference between η and the "true" value η^o, re-evaluated and plotted by Lowe (Lo76), was significant only for η^o near 0 and 1 and could be characterized by the ratio Δ_{zz}/V_{zz}. It is sufficiently large to account for the change shown in the simulation.

An undistorted pentagonal bipyramid has no EFG asymmetry at it's center. It seems unlikely however that the two low temperature sites differ only by the degree of distortion as point b) illustrates this would not account for the large differences in the observed interaction frequencies.

The increase in η for site B between 160 and 250 K can be interpreted as a change in the relative populations, p_1 and p_2, of two states for the hafnium atom characterized with different asymmetries and the same fundamental frequency (such as two different levels of pentagon distortion). The observed asymmetry is an average of the two:

$$\eta(T) = (1-p_2(T))\,\eta_1 + p_2(T)\,\eta_2 \tag{6-4}$$
$$= \eta_1 + (\eta_2 - \eta_1)p_2(T).$$

The population ratio is given by the Boltzmann distribution

$$\frac{p_1(T)}{p_2(T)} = \frac{g_1}{g_2}\,e^{-E/kT}, \qquad \frac{g_1}{g_2} = \frac{\eta_2 - \eta_1}{\eta_m - \eta_1} - 1 \tag{6-5}$$

where E is the energy difference between the states and g_1, g_2 and η_m are the high temperature limits of the two relative populations and the maximum observed asymmetry. Defining T^o as the mid point temperature of the asymmetry change, equation (6-4) becomes

$$\eta(T) = \eta_1 + \frac{\eta_2 - \eta_1}{1 + (g_1/g_2)e^{E/kT}}, \tag{6-6}$$

and

$$E = kT^o \ln(2 + g_2/g_1).$$

The maximum and minimum degeneracy ratio and the corresponding energy difference compatible with the observed data (figure 6-13) are:

	g_1/g_2	E
max.	10^{-5}	.18 eV
min	10^{-8}	.30 eV

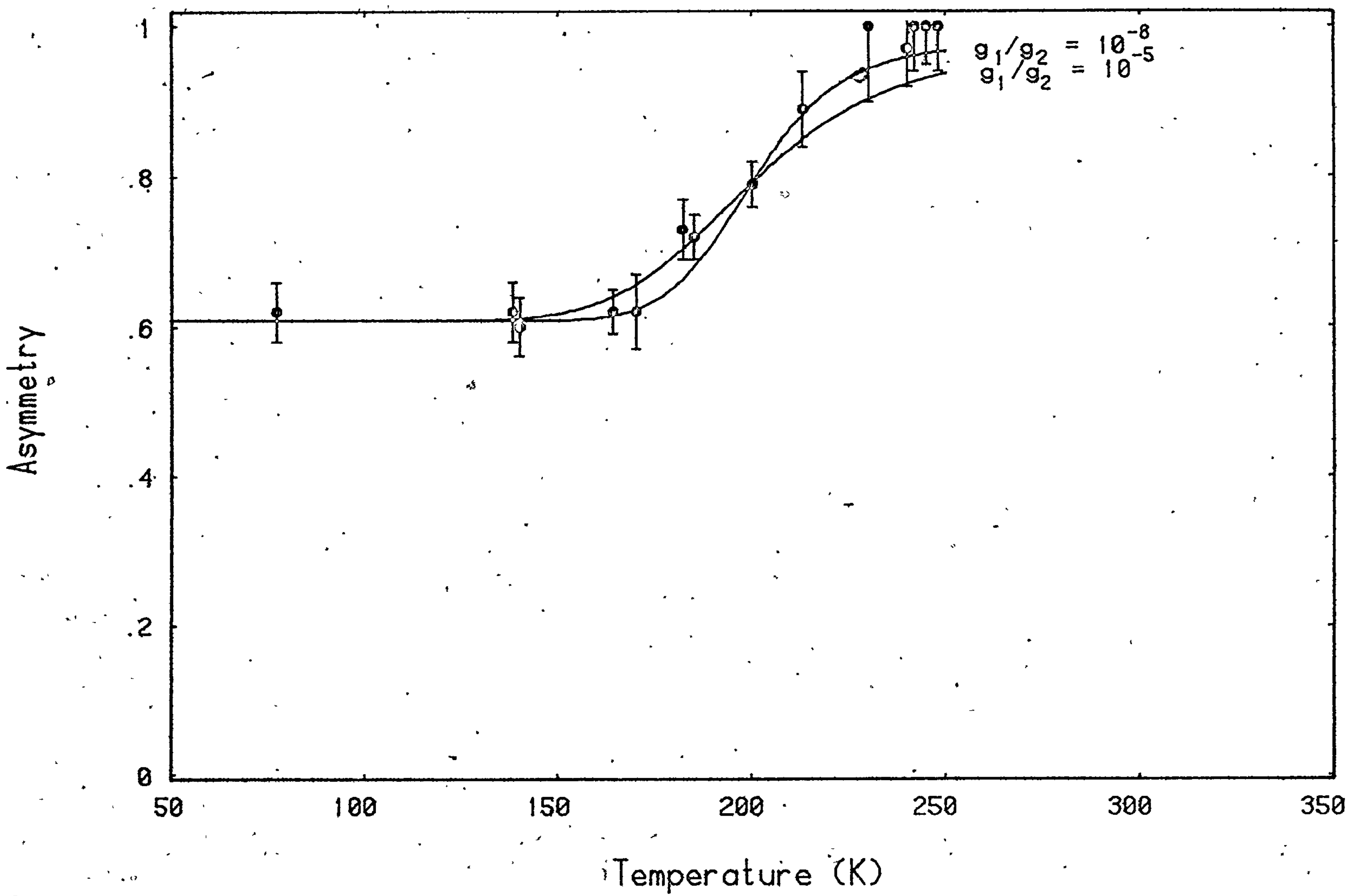

Figure 6-13. Comparison of measured site B asymmetry with the two state model (equation 6-6).

Thus this model of a rare, higher energy second state for the site B hafnium will correctly describe these results. Such a state could be due to a chemical impurity or (although less likely) radiation damage from neutron bombardment during sample activation. All observed states must be stable because the sample temperature was periodically raised and lowered between 77 and 300 K over a period of many months and the perturbation factor showed a consistent temperature dependence.

The relaxation term in the high temperature phase, λ, appeared to show some decrease with increasing temperature, although the large uncertainties precluded any definitive conclusion. Boyer et al. (Bo76) studied the similar compound Na_3HfF_7 and observed a comparable two to one site transition between 375 and 455 K, above which the dynamic interaction relaxation showed the form

$$\lambda_2(T) = \lambda_2^{\infty} e^{(E_a/kT)} \qquad (6\text{-}4)$$

where E_a is an activation energy of 0.13 ± .03 eV and λ_2^{∞} is of order .001 ns^{-1}. The temperature range above the transition covered in the present study is too small to show conclusively whether a similar dynamic interaction process occurs in K_3HfF_7. E_a was evaluated to be < 0.05 with a 95% confidence level which strongly suggests it is less than in Na_3HfF_7. The λ_2^{∞} value was 0.1 ± .4 ns^{-1}.

CHAPTER 7

CONCLUSIONS

The deconvolution analysis showed that while this procedure correctly reconstructs the high frequency detail of the perturbation factor, it does not allow the fitted parameters, namely ω_1, η and δ to be determined with any improvement in accuracy. The benefits gained by fitting the data to a model without the attenuation factor representing finite time resolution is offset by the greater uncertainties associated with the attendant higher spectral noise content. Both the experimentally determined values and the corresponding statistical uncertainties remain virtually unchanged. There is merit in knowing that the spectral components masked from the model by the time resolution term are real, and appear in the measured data after a deconvolution process. This builds confidence that the correct model has been used. The Bayesian technique of deconvolution was shown to introduce less noise than the linear transform approach.

Deconvolving the time-interval spectra allowed a more accurate estimate of the true time zero channel. It was discovered that the traditional method of choosing the half maximum point produced an error of one channel, corresponding to one sixth of the standard deviation time resolution term. This is a small error but was responsible for an undesired decrease in the perturbation factor observed in the channels closest to time zero. Making this correction had a negligible effect on the evaluated parameter values.

The study on the K_3HfF_7 polycrystalline sample confirmed the results of Lowe (Lo77) that a one site model for the hafnium atom can be fitted to the data collected at room temperature and a two site model is required to fit the 77 K data. The change takes place very abruptly at a critical temperature of 250 ± 1 K. The population ratio of the low temperature sites was 3:1.

The asymmetry of the lesser populated site below 250 K increased from 0.62 to 1.0 between 160 and 240 K. This change is compatible with a two state model for this site in which the energy difference is approximately 0.2 eV and the degeneracy ratios are between 10^{-5} and 10^{-8} in favour of the lower energy state. These states can be explained as having different degrees of distortion in a distorted pentagonal bipyramid model for the HfF_7^{3-} ion.

BIBLIOGRAPHY

Ab53 A. Abragam and R.V. Pound, Phys. Rev. 92(1953)943

Al52 K. Alder, Helv. Phys. Acta 25(1952)235

An70 P. da R. Andrade, A. Vasquez, J.D. Rogers and E.R. Fraga, Phys. Rev. B, 1(1970)2912

Ba74 Chr. Bargholtz, Nucl. Instr. and Meth., 120(1974)121

Be69 R. Beraud, I. Berkes, J. Daniere, G. Marest and R. Rougny, Nucl. Instr. and Meth., 69(1969)41

Bi53 L.C. Biedenharm and M.E. Rose, Rev. Mod. Phys. 25(1953)729

Bi64 J.B. Birks, *The Theory and Practice of Scintillation Counting*, Pergamon Press, New York (1964)

Bo70 J.F. Boulter, W.V. Prestwich and T.J. Kennett, Nucl. Instr. and Meth., 77(1970)163

Bo71 J.F. Boulter, Ph.D. Thesis, McMaster University (1971)

Bo76 P.Boyer, O. de O. Damasceno, O. de Fabris, J.R.F. Ferreira, A.L. de Oliveira and J.J. de Oliveira, J. Phys. Chem. Solids, 37(1976)1019

Br78 R.N. Bracewell, *The Fourier Transform and its Applications*, McGraw-Hill Book Company, Toronto (1978)

Bu71 Y.A. Buslaev, V.I. Pachomov, V.P. Tarasov and V.N. Zege, Phys. Stat. Sol. (b) 44(1971)K13

Co66 F.A. Cotton and G. Wilkinson, *Advanced Inorganic Chemistry*, Wiley-Interscience, Inc., New York (1966)p135

Da59 W.C. Davidon, Argonne National Laboratory report no. ANL-5990 Rev. (1959)

Do70 S. Donati, E. Gatti and V. Svelto, Nucl. Instr. and Meth., 77(1970)179

Do74 R.C. Dorf, *Modern Control Systems*, Addison-Wesley Publishing Company, Don Mills (1974)

Fl63 S.R. Fletcher and M.J.D. Powell, Comp. J., 6(1963)163

Fo71 M. Forker and J.D. Rogers, Nucl. Instr. and Meth., 96 (1971)453

Fo73 M. Forker, Nucl. Instr. and Meth., 106(1973)121

Fr51 H. Fraunfelder, Phys. Rev. 82(1951)549

Fr68 H. Frauenfelder and R.M. Steffen, Ed. K. Siegbahn, *Alpha-, Beta- and Gamma-Ray Spectroscopy*, Vol. 2, North Holland Publishing Company, Amsterdam (1968)

Ga69 P.R. Gardner, M.Sc. Thesis, McMaster University (1969)

Ga70 P.R.Gardner and W.V. Prestwich, Can. J. Phys. 48(1970)1430

Ge69 E. Gerdau, J. Wolf, H. Winkler and J. Braunsfurth, Proc. Roy. Soc. (London), A311(1969)197

Ge71 E. Gerdau, B. Scharnberg and H. Winkler, *Hyperfine Interactions in Excited Nuclei*, Eds. G. Goldring and R. Kalish, Gordon and Breach, New York 1971 p861

Ge73 E. Gerdau, J. Birke, H. Winkler, J. Braunsfurth, M. Forker and G. Netz, Z. Phys. 263(1973)5

Go46 G. Goertzel, Phys. Rev., 70(1946)897

Ha38 G.C. Hampson and L.Pauling, J. Chem. Soc. 60(1938)2702

Ha59 L.A. Harris, Acta Cryst. 12(1959)172

Hs70 H.P. Hsu, *Fourier Analysis*, Simon & Schuster Inc., New York (1970) p13

Hu70 H.J. Hurst and J.C. Taylor, Acta. Cryst., B26(1970)417

Ka71 E. Karlsson, *Angular Correlations in Nuclear Disentegrations*, Eds. H. van Krugten and B. van Nooijen, Rotterdam University Press, Groningen, The Netherlands (1971) p27

Ke78a T.J. Kennett, W.V. Prestwich and A. Robertson, Nucl. Instr. and Meth., 151(1978)285

Ke78b T.J. Kennett, W.V. Prestwich and A. Robertson, Nucl. Instr. and Meth., 151(1978)293

Ke78c T.J. Kennett, P.M. Brewster, W.V. Prestwich and A. Robertson, Nucl. Instr. and Meth., 153 (1978) 125

Ke79 T.J. Kennett, W.V. Prestwich, Phys. Med. Biol., 24, 6(1979)1107

Lo76 L.M. Lowe, Ph.D. Thesis, McMaster University (1976)

Lo77 L.M. Lowe and W.V. Prestwich, Chem. Phys. Let. 46 (1977)531

Ma63 E. Matthias, W. Scheider and R.M. Steffen, Phys. Let. 4(1963)41

MK68 B.T.A. McKee, Nucl. Instr. and Meth., 62(1968)13

Pr62 M.A. Preston, Physics of the Nucleus, Addisson-Wesley Publishing Company, Reading Mass. (1962) 315

Ra63 J.C. Raich and R.H. Good Jr., Am. J. Phys., 31(1963)356

Re70 K.Rama Reddy, Nucl. Instr. and Meth., 81(1970)183

Ri79 H.H. Rinnberg, Atom. Ener. R. 17 (2)(1979)477

Ro53 M.E. Rose, Phys. Rev., 91 3(1953)610

Ro59 M. Rotenberg, R. Bivins, N. Metropolis and J.K. Wooten Jr., The 3-j and 6-j Symbols, Technology Press, M.I.T., Cambridge (1959)

Si67 B. Sigfridsson, Nucl. Instr. and Meth., 54(1967)13

St64 R.M. Steffen and H. Frauenfelder, Perturbed Angular Correlations, Eds. E. Karlsson, E. Matthias and K. Siegbahn, North Holland Publishing Co., Amsterdam, (1964) p18

St64a R.M. Steffen and H. Frauenfelder, Ibid, p40

St64b R.M. Steffen and H. Frauenfelder, Ibid, p25

Ta69 V.P. Tarasov and Y.A. Buslaev, Zh. Struct. Khim. 10(1969)816

Wa69 H.F. Wagner and M. Forker, Nucl. Instr. and Meth., 69(1969)197

Wa70 M.A. El-Wahab and M.A. El-Salam, Nucl. Instr. and Meth., 78(1970)325

Wi73 H. Winkler and E. Gerdau, Z. Phys. 262(1973)363

Za54 W.H. Zachariasen, Acta Cryst. 7(1954)792

APPENDIX I

THE QUADRUPOLE INTERACTION HAMILTONIAN

The quadrupole interaction causes a hyperfine splitting of the nuclear magnetic levels as a function of the electric field gradient asymmetry η. For the spin = 5/2 state the interaction energies are given by solutions (Be69) to

$$W^3 - 28W(\eta^2 + 3) + 160(\eta^2 - 1) = 0$$

which are

$$\begin{aligned} E_{\pm 5/2} &= 2\alpha\hbar\omega_Q \cos(\tfrac{1}{3} \arccos \beta) \\ E_{\pm 3/2} &= -2\alpha\hbar\omega_Q \cos(\tfrac{1}{3} (\pi + \arccos \beta)) \\ E_{\pm 1/2} &= -2\alpha\hbar\omega_Q \cos(\tfrac{1}{3} (\pi - \arccos \beta)) \end{aligned} \qquad (I-1)$$

where

$$\alpha = \sqrt{\frac{28}{3} (3 + \eta^2)}$$

$$\beta = \frac{80(1-\eta^2)}{\alpha^3}$$

giving
$$\begin{aligned} \omega_1 &= 2\sqrt{3}\ \alpha\ \omega_Q \sin(\tfrac{1}{3} \arccos \beta) \\ \omega_2 &= \alpha\ \omega_Q (3 \cos(\tfrac{1}{3} \arccos \beta) - \sqrt{3} \sin(\tfrac{1}{3} \arccos \beta)) \\ \omega_3 &= \omega_1 + \omega_2 \end{aligned} \qquad (I-2)$$

Equation (I-2) can be rearranged to find the interaction frequency ω_Q from the measured ω_1 and η values.

APPENDIX II

SIMULATION OF AN ELECTRIC FIELD GRADIENT FROM A POINT CHARGE DISTRIBUTION

The electric field gradient resulting from a point charge distribution is obtained by differentiating the expression for the electric potential with respect to the coordinate axes twice. The potential at the origin from one point charge with position vector $\vec{r}$ is

$$V = \frac{-e}{4\pi\varepsilon_0 r} \qquad \text{(II-1)}$$

and the general form of the field gradient is

$$V_{ij} = \frac{d^2V}{dx_i dx_j} = \frac{3x_i x_j - \delta_{ij} r^2}{r^5} \frac{e}{4\pi\varepsilon_0} \qquad \text{(II-2)}$$

where x_i, x_j represent any two of the independant Cartesian coordinates (x, y and z) and δ_{ij} is the delta function. Contributions from each point charge are summed.

The resulting V_{ij} matrix must be diagonalized to define an orthogonal set of axes so that $/V_{zz}/ \geq /V_{xx}/ \geq /V_{yy}/$. The asymmetry and interaction frequencies can be calculated using equations (2-8) and (I-2).